Measuring Material Properties of Proton Exchange Membranes using Pressure Loaded Blister Testing and Digital Image Correlation

Chase Michael Siuta

Thesis submitted to the faculty of the Virginia Polytechnic Institute and State University in partial fulfillment of the requirements for the degree of

Master of Science
In
Engineering Mechanics

Scott W. Case
David A. Dillard
Michael W. Ellis
Yongqiang Li

August 11, 2011
Blacksburg, Virginia

Keywords: proton exchange membrane, digital image correlation, pressure-loaded blister test, biaxial strength, linear damage accumulation, PFCB, hydrocarbon membrane

Measuring Material Properties of Proton Exchange Membranes using Pressure Loaded Blister Testing and Digital Image Correlation

Chase Michael Siuta

ABSTRACT

The strength and durability of proton exchange membranes for use in fuel cells has received much attention recently due to the increased push for sustainable alternatives to the internal combustion engine. To be viable, these alternatives must have comparable lifetimes and power outputs to the internal combustion engines they replace. Chemical degradation was once viewed as the most common culprit of early fuel cell failure, but as membranes and catalysts improved, mechanical failure became an important factor. As a result, fundamental research on the mechanically-induced failure mechanisms of fuel cell membranes, coupled with development and processing of less expensive membranes, has become an important topic. The use of the blister test geometry, along with digital image correlation of the deformed shape, creates a self-contained analysis tool useful for measuring the biaxial strength of membranes. In this work, blister tests are used to measure biaxial stress and strain for fuel cell membranes subjected to ramped pressure loading to form stress-strain curves that indicate the onset of yielding under biaxial stress conditions. Stress-life curves are developed experimentally for Gore-Select® series 57 members using data collected under constant pressure conditions. These results are used to predict blister failure under ramped and fatigue loadings. A newly implemented hydrocarbon membrane system is evaluated with constant-pressure-to-leak blister testing. Improved strength following an isothermal hold at 100°C (pretreatment) is shown to occur. Ramped pressure testing indicates that the material after the pretreatment is stiffer and has a higher yield stress than the material before treatment. Morphological and constitutive characterization indicated differences in the materials that are consistent with the improved performance.

ACKNOWLEDGEMENTS

In this unfairly brief section, I would like to cram in the many people that I want to recognize for helping me through this research project. First off, I would like to thank my advisor Dr. Scott Case, for never audibly complaining about the many times I went into his office with new problems, and for helping me solve them every time that I did. I would like to thank the Engineering Science and Mechanics department for the education and the opportunities that they provided for me and the Institute for Critical Technology and Applied Science (ICTAS) for providing and maintaining an excellent laboratory workspace. I would like to thank Dr. David Dillard and his research group for allowing me honorary member status for much of my research career and putting up with my attendance at their group meetings. I would like to thank the rest of my committee members for raising and answering questions throughout the data collection and analysis process, as well as for reading my thesis, which having written it I know is no easy task. I would like to thank the members of the GM Electrochemical Energy Research Lab for allowing me this opportunity to work with them on forming new ideas and solutions that may one day help implement fuel cell vehicles on a global scale. I would like to thank my family for their ongoing support of me, probably giving me way more credit than I am due, but for that I am grateful. And finally, I would like to thank the GM group at Virginia Tech, both past and present members, for the time that we have all spent working together in the lab and outside of it. It has been an honor to get to know all of you and I have little doubt that it is you all that have so far kept me sane.

Table of Contents

List of Figures

List of Tables

Chapter 1: Introduction

Motivation for Research

Proton exchange membrane fuel cells (PEMFCs) are a promising mobile alternative to internal combustion engines. However, PEMFCs remain complex chemical, electrical, and mechanical systems that operate through temperature and humidity fluctuations. In order for the fuel cell to be a commercially viable option, it must retain many qualities that the typical consumer has become used to, such as the ability to operate in a wide range of external conditions, comparable power output to a combustion engine, and comparable lifetime durability. In 2010, the cost of the fuel cell in the transportation industry was brought down to $61/kW, decreasing the cost to less than 25% of what it had been in 2002 [1]. The reported lifetimes have also improved, with an operational lifetime in a transportation environment of approximately 2500 hours. However, these numbers must continue to improve in order to meet the Department of Energy's goal of $30/kW and 5000 hours of operation time above 60% efficiency by 2015, finally bringing the fuel cell into serious competition with internal combustion engines. To further complicate matters, fuel cells must sustain this performance over the full range of operating temperatures (-40°C to 120°C).These two fundamental issues, durability and cost, are the main chokepoints for widespread fuel cell use in transportation [1].

The basic components of a fuel cell are a proton exchange membrane (PEM), a catalyst layer, and a gas diffusion layer (GDL) sandwiched between two bipolar plates that contain flow channels. The catalyst layer is a mixture of carbon black, platinum, and an ionomeric solution (most commonly Dupont's Nafion® solution) that is applied to either side of the PEM, generally no thicker than 25 microns, to form a membrane-electrode assembly (MEA). The GDL is a porous media used to further disperse the reactant gases, hydrogen and oxygen, evenly across the surface of MEA, in addition to providing electrical and thermal conduction as well as managing water transport. The flow channels function similarly while carrying the hydrogen gas to the anode side of the MEA and air to the cathode side of the MEA [2]. A schematic representation of a fuel cell is shown in Figure 1-1.

Figure 1-1: Basic schematic of a fuel cell. Not shown to scale.

The surface of the MEA is where the electrochemical half-reactions, shown in Eqn. 1.1, take place.

$$H_2 \leftrightarrow 2H^+ + 2e^-$$
$$\frac{1}{2}O_2 + 2H^+ + 2e^- \leftrightarrow H_2O \qquad\qquad 1.1$$
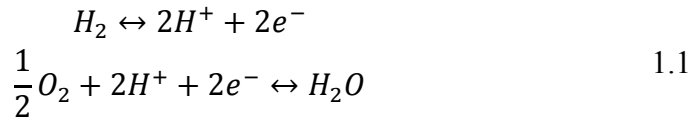
These are the fundamental reactions behind a fuel cell and it should be recognized as a two-step combustion reaction of hydrogen. However, during the combustion of hydrogen, these two reactions occur in the same area and no electrical energy is produced, as the hydrogen ions and electrons combine to form water molecules. However, by separating the reactions onto either side of the MEA with an electrolyte, in this case a PEM, the electrons are forced to pass through an external circuit and current is produced. The hydrogen ions (protons) are allowed passage to the cathode side through the proton conducting electrolyte, allowing the completion of the reaction and the formation of the only byproduct, water [2].

In an operating fuel cell, the bipolar plates, which allow the gases to reach the reactant sites, are compressed onto either side of the MEA, leaving portions of the MEA underneath the plates completely constrained while other portions are free to expand and contract in the flow channels. The most common PEMs used in these commercial MEAs are perfluorosulfonic acid (PFSA) membranes such as Nafion®, which has been the staple membrane in the commercial fuel cell business since it was created by Dupont in the 1960s [3]. Its popularity is due in large part to its low permeability to hydrogen and oxygen and its high proton conductivity. The structure of Nafion® is unique in that it contains sulfonated hydrophilic side chains and a hydrophobic backbone that becomes oriented into channels to facilitate proton conductivity [4]. For peak efficiency in proton conduction, the membrane requires significant hydration, and PFSA materials show large mechanical property changes with the addition of moisture [5,6,7]. Multiple studies have been performed on water uptake of Nafion® under different relative humidity conditions [5,8,9] that show significant amounts of water uptake and in turn lead to large dimensional changes [5]. In an automotive application, the material is expected to undergo fluctuations in temperature and humidity that can range from ambient conditions while not being used to 120°C and 150% relative humidity during operation [10], and throughout operation the membrane may undergo smaller fluctuations based on the power consumption of the vehicle. Dimensional changes in unconstrained Nafion® can be on the order of 15% in cases of large shifts in humidity [11].

It is apparent that the changing conditions, coupled with the significant water uptake of PEMs and the constraint between the bipolar plates that does not allow for the wanted expansion, leads to stress duty cycles in the membrane. Compressive stresses that appear during hydration begin the process of viscoelastic relaxation that leads to higher tensile stresses during dehydration. This behavior of a constrained viscoelastic material was demonstrated with thermal cycling of adhesives by Humfeld and Dillard [12]. As an added complication, the viscoelastic nature of the material makes quantifying the induced stresses a time-dependent problem [6]. It is important to note that other membrane systems, specifically hydrocarbon structures, have been

investigated but Nafion® remains the benchmark PEM in durability and performance in a fuel cell [10].

Because of the hygrothermal stress fluctuations that occur throughout the lifetime of the fuel cell, cracks and pinholes begin to form that allow for hydrogen to crossover and greatly decrease the efficiency of the cell [6,11]. The effect that pinholes have on a cell was explored by Lu et al. [13], who showed that pinholes formed in the MEA led to a more rapid decline in performance of the cell and a significant decrease in open circuit voltage over time. This reduction in open circuit voltage can be related to hydrogen crossover, which occurs when hydrogen gas does not react at the anode but flows from the anode side to the cathode side through a crack. Lai and Dillard [10] presented postmortem cross sections of failed PEMs after relative humidity (RH) cycling that show multiple cracks forming in the membranes, seen in Figure 1-2. Humidity was cycled from 0-150% RH, with two minutes at each condition. For this test method, failure was defined as a 10 sccm (standard cubic centimeters per minute) crossover leak rate of air through the sample, which is detrimental to cell performance.

(a)   (b)
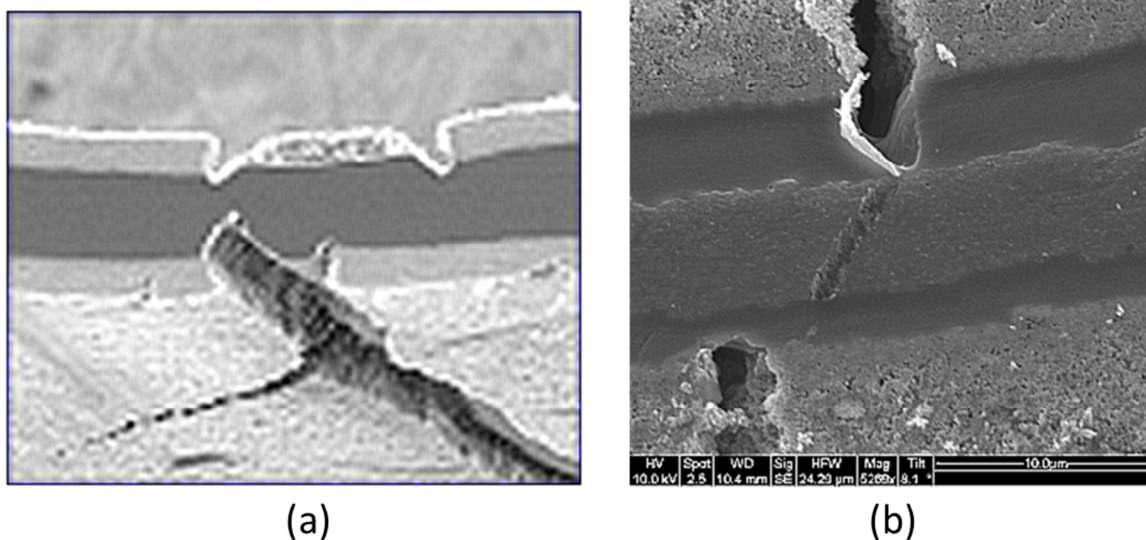
Figure 1-2: Representative postmortem cross-sectional micrographs of three commercially available PFSA membranes (a) Nafion® NR-111and (b) Gore-Select® series 57

There has been increasing effort in understanding and characterizing the evolution of such cracks and pinholes over the lifetime of PEMs. Multiple modeling efforts have gone into measuring and modeling the effect of hygrothermal loading on PEMs constrained in a fuel cell. Liu et al measured cell degradation over time for a fuel cell loaded under cyclic current loading. It was found that pinhole failure leading to hydrogen crossover was the dominant failure mechanism [14].Tang et al. have shown that the stresses in the material are predominantly in-plane biaxial using a hygrothermoelastic constitutive model [11]. Lai et al. have had significant success modeling the membrane as a linear viscoelastic material using finite element analysis. Much of the data was characterized using a dynamic mechanical analyzer (DMA) under relaxation and creep mode in the linear range of the material [6]. Silberstein et al. have included

a viscoplastic term for modeling Nafion® in the biaxial state under large loadings. This viscoplastic behavior was experimentally investigated using biaxial testing done on cruciform specimens pulled to strains on the order of 50% [15]. Patankar et al. characterized Nafion® PEMs as nonlinear viscoelastic using the Schapery hereditary integral model, and they were successfully able to apply the model to multiple loadings [16]. Li has applied a method of bimaterial curvature to successfully capture experimentally the biaxial stresses induced in a material under constrained hygrothermal loading [17,18,19]. The over-arching goal behind all of this fundamental research is to be able to take the hygrothermal stress histories, either experimental or modeled, and correlate them with material strength measurements to predict membrane failure in a fuel cell.

The mechanical strength of PEMs has been analyzed in multiple different ways. Research conducted at General Motors has shown that cycling PEMs through humidity conditions in a constrained fuel cell without chemical reactions taking place will still cause failure in the membrane [10,20]. It is difficult to experimentally measure the stress induced in a membrane during this humidity cycling procedure, and the multiple replicates necessary to have confidence in strength data would take thousands of hours. Much of the strength data on PEMs is therefore based on ex-situ uniaxial tension data that extends past yield and to failure [21]. Tang et al. analyzed the breaking stress and proportional limit stress of Nafion® at varying humidity and temperature under uniaxial tension. The breaking stress did not show a definite trend with humidity changes, while the proportional limit stress consistently decreased with increased humidity [5]. While uniaxial tension is a widely popular method for measuring strength of numerous different materials, it is unclear whether the failure mode in a fuel cell (where the stress is biaxial) is directly comparable. In addition to strength characterization, knife slit testing has been used by Patankar et al. on three types of Nafion® membranes to characterize the fracture energy of the material under different humidity and temperature conditions. While this data is useful in qualitatively expressing material durability through comparisons to other materials, the connection to hygrothermal cycling and induced stresses is not obvious [22,23]. Pressure and volume loaded blister testing has been employed extensively as a strength test by the GM-VT group [24,25,26,27]. The blister test (or bulge test) is unique in that it both mimics the pinhole failures and the biaxial stress state observed in working fuel cells. However, the stress state in proton exchange membrane blisters is complex, time dependent, and is not well understood. This has led to varying degrees of approximations being made to attempt to quantify and better understand the failure data accumulated. A linear elastic solution to the blister problem was solved analytically by Hencky [28] and used as a linear quasi-elastic stress approximation by Dillard et al. [24] with good success. A linear viscoelastic approximation was presented by Grohs et al. [25] by converting the linear elastic solution to a linear viscoelastic solution using Alfrey's correspondence principle [29]. Finite element modeling was also used with a linear viscoelastic constitutive model to varying degrees of accuracy [30]. While these models showed promise, they acknowledged the extension of a linear, small strain constitutive model to a large strain application.

Thesis Layout and Focus of Research

The intent of this research was to examine the use of the blister test coupled with digital image correlation to measure biaxial material strength, with the goal being the elimination of major analytical assumptions. This would make DIC blister data an excellent outside comparison to modeling data; effectively approaching the same problem from two sides and making sure that they agree. While this thesis does not contain (finite element) modeling, the capability of the DIC blister data to stand alone still remains important for the testing that was completed and tests that may be looked at in the future. The use of DIC and blister tests can be used as an integrated material strength characterization tool for fuel cell membrane materials and MEAs. Its use solves the main issue of previous blister testing: the extent of deformation and the timescale on which it operated was unknown. This is no longer the case, and efforts can be made to examine the blister test in a whole new light. This is important since the blister test has been shown to be an excellent method for leak detection in both PEMs [24] and MEAs [31]. Directly using gas leakage as the failure criterion connects the in-situ and ex-situ failure modes.

This thesis has been assembled as a collection of three publication-ready papers. Although they are written as separate papers, they are interconnected in the experimental methods that they use and the analysis techniques that they develop. The first paper, presented in Chapter 2, is an introduction to using digital image correlation on the blister test, and it provides a full insight into the development of the method as well as the expected data output and accuracy. The second paper, presented in Chapter 3, examines the use of digital image correlation and the blister test to experimentally determine lifetime prediction parameters of a commercially available PEM (Gore-Select® series 57) and apply them to various pressure-loadings. (Chapter 3 has already been accepted for the ASME 2011 5th International Conference on Energy Sustainability and 9th Fuel Cell Science, Engineering and Technology Conference.) The final paper, presented in Chapter 4, makes comparisons of the biaxial strength of an in-development PEM blended (70% hydrocarbon/30% rubber) system. It focuses on the difference found in the material system TAKS115C BR10 cast at a commercial coater. In all of the previously mentioned papers, the blister test was used in accordance with digital image correlation to quantify material properties under biaxial loading.

Chapter 2: Using Digital Image Correlation to Measure Time Dependent Biaxial Deformation of Proton Exchange Membranes during Pressurized Blister Testing

Abstract

A 3D digital image correlation technique for use with blister testing of PEMs is outlined. The PEMs were tested under temperature and humidity conditions typical of fuel cell environments with the use of an environmental chamber with a glass door. Problems with measuring the deformation of thin, translucent or transparent PEMs using digital image correlation were found to be shortened lifetimes attributed to the speckling procedure, lack of speckle contrast due to membrane transparency, and data loss at reflective "hot spots" from large deformations. The shortening of lifetimes was corrected by employing the use of an airbrush and India ink to do the speckling instead of traditional spray paints. Membrane transparency and the data loss from reflection were both overcome by the development of a new fixture capable of being lit from the back using fiber optics. Full field deformation of the blister sample was captured, which allows the calculation of principal strains, principal directions, and stress approximations. The measured deformation includes strain near 150%.

Introduction

Fuel cells are a promising new alternative to gasoline powered engines in automobiles. At the heart of these fuel cells are proton exchange membranes (PEMs) that conduct protons from the anode to the cathode side of an electrochemical reaction while forcing electrons to travel around, creating a current and producing usable electrical energy [2]. Such PEMs generally range from 10-30 μm in thickness. One of the continuing shortcomings of PEM fuel cells is their durability, for which the DOE has placed a benchmark of over 5000 hours of operation by 2015 [1]. Although chemical durability has been the focus in the past, improvements in this area have shifted the focus towards mechanical durability. Studies have shown pinhole failures in fuel cell stacks subject to hygrothermal cycling analogous to cycles seen in an automobile duty cycle [20]. Due to the constrained nature of the membrane in the fuel cell, this cycling induces a biaxial stress state in the material [10] and eventually leads to leaks in the membrane that greatly reduce the cell efficiency [13]. Because of such findings, it is important to be able to understand and quantify the biaxial behavior of PEMs.

Analysis of the biaxial behavior of PEMs, specifically Nafion®, has been documented by Silberstein and Boyce [15] using a cruciform test with laser cut samples. With this method both stress and strain can be measured in a similar manner to that of uniaxial tension testing. Blister testing of PEMs has been used extensively by Dillard et al. [24,25,30,27] to quantify material strength, specifically the resistance to the mechanical formation of pinholes under a state of biaxial stress and strain. Hencky presented an analytical solution to the stress and displacement profiles in the circular bulge test by solving an axisymmetric static force balance differential equation using an infinite series solution [28]. In the previous works this solution provided an

analytical guide to the stresses seen in the center of the membrane by assuming quasi-elastic behavior [24]

$$\sigma_{center}(t) = \frac{B_0}{4}\left[\frac{p(t)^2 \cdot a^2}{{h_0}^2}E(t)\right]^{1/3} \qquad 2.1$$

and linear viscoelastic behavior using the Boltzmann superposition integral [25].

$$\sigma_{center}(t) = \frac{B_0}{4}\left[\frac{a}{h_0}\right]^{\frac{2}{3}}\int_0^t E(t-\tau)^{\frac{1}{3}}\frac{dp(\tau)^{\frac{2}{3}}}{d\tau}d\tau \qquad 2.2$$

In the previous equations, B_0 is a constant dependent on Poisson's ratio, a is the radius of the bulge test opening, p is pressure, h_0 is the initial material thickness, and E is the material's modulus.

However, major assumptions must be made to utilize such a model that does not account for the large creep strains seen during loading. Indeed, the material properties must be previously known, making a direct experimental comparison to other biaxial data impossible.

Deformation measurements of bulge tests, since it has been classically used for testing linear elastic behavior, have been focused on measuring bulge height at the bulge center and using it in accordance with the formula obtained by Vlassak and Nix [32]. Measurements have been performed using multiple optical techniques, such as a calibrated vertical displacement method [33], laser interferometry [32], and other techniques that require highly smooth and reflective surfaces to capture light reflecting off the membrane surface [34]. Xu and Liechti have recently implemented Moiré deflectometry to measure the curvature of circular and rectangular bulge tests of 3 μm polyethylene terephthalate (PET) film [34]. For the circular bulge the stress was then approximated from thin-walled spherical pressure vessel theory at the center, given in Eqn. 2.3.

$$\sigma = \frac{pR}{2h} \qquad 2.3$$

where p is the applied pressure, R is the radius of curvature, and h is the thickness of the membrane. The Moiré deflectometry technique is useful in that it allows for the measurement of transparent and non-reflective films; however, it requires significant differences in the refractive index of the media on either side of the bulge (e.g. in [34] the pressurization medium was water) and significant deformation information is lost by only capturing central curvature, since the deformation measurements are not full field.

The goal of this research was to devise and implement a method of full field deformation measurement using digital image correlation that could experimentally measure the stress and strain behavior of the blister test in a comparable manner to that of a uniaxial tension test or a

biaxial cruciform test. This would provide a basis for comparison of future analytical models. It would also improve the utility of the blister test method by incorporating both biaxial material strength (with a gas leakage failure criterion) and biaxial material constitutive behavior together.

Digital Image Correlation

The use of DIC is becoming quite popular in experimental mechanics. There are many uses for which it has shown applicability. Federov et al. have made use of the technique in delamination experiments [35]. Jin et al. have used DIC on the micro-scale to look at deformation under scanning electron microscopy [36]. Li used the DIC to measure of deformation during RH cycling of a membrane bonded to a substrate and calculated the induced stresses in the membrane using the method of bimaterial curvature [17]. This is because it is a versatile, non-invasive technique to measure localized deformation of samples with irregular shapes or structures that may otherwise be directly immeasurable. This is the case for thin films, where strain gauges and extensometers cannot be used.

Throughout this work, the GOM ARAMIS® version 6 software is used together with Schneider-Kreuznach cameras with a resolution of 1200 by 1600 pixels equipped with 50mm lenses. The following explanation of digital image correlation, although it is in most cases a general procedure, will be based upon methods developed using this software. 3-D DIC works by comparing images of the same specimen taken from two separate cameras placed at an angle from each other. This comparison not only allows the measurement of 2-D deformation, which can be done with a single camera, but also calculates the deformation out of the camera plane. To track the deformation, a random pattern must be applied to the sample. This pattern gives a sense of visual uniqueness to each region of the material and allows for those regions to be tracked. Each separate region computationally corresponds to a facet, a box of pixels enclosing the random pattern of a single region that can vary in size and spacing, and may even overlap depending on the user's definition.

Each facet center provides a data point in a global X, Y, Z coordinate system. To calculate strain a square *2n+1* x *2n+1* matrix (for *n≥1*), surrounding and including the analyzed point, is collected (e.g. the default setting in ARAMIS is a 3x3 matrix). From this matrix the deformation gradient is calculated for the central facet and can then be used to calculate other necessary deformation information in any reference frame. The strain coordinate system always runs tangent to the surface of the material so that the X strain direction is parallel to the X-Z plane and the Y strain is perpendicular to the X strain. The principal directions and the principal stretch ratios on the surface can be found by rotating the strain with Mohr's circle using Eqn. 2.4.

$$\lambda_{1,2} = 1 + \frac{\varepsilon_x + \varepsilon_y}{2} \pm \sqrt{\left(\frac{\varepsilon_x + \varepsilon_y}{2}\right)^2 - det(\boldsymbol{\varepsilon})} \qquad\qquad 2.4$$

From these principal stretches, many different common strain measurements can be calculated [37]. It is important to realize that no through thickness information is captured since this is a surface technique.

In this work, a facet size of 21x21 pixels was used, with a center to center separation (step size) of 10 pixels, giving approximately 50% overlap. Calibration was performed through the glass oven door to incorporate the changes in light caused by the glass. The ARAMIS software package quotes out-of-plane accuracy to be $3x10^{-5}$ times the field of view. The field of view for this work was 25x20 mm and from that the theoretical displacement accuracy is predicted to be on the order of 1 micron ($25 \times 3x10^{-5}$).

The ability to capture and fit a given geometry was briefly investigated by measuring a sphere of known diameter. The spherical geometry was chosen as it corresponds closely to the shape of a deformed blister, and the size of the sphere was chosen to be very near the diameter of the blister fixture (19 mm). The sphere was measured to have a diameter of 20.05 mm using a drop gauge micrometer and was then speckled and measured using the DIC. By fitting a sphere to the DIC data using a least squares approach, an option that is included in the ARAMIS software package, the diameter was measured to be 20.068 mm, a difference of 0.0898%. The process is shown in Figure 2-1. The accuracy of the spherical fit increases the confidence in the geometric measurements of the system.
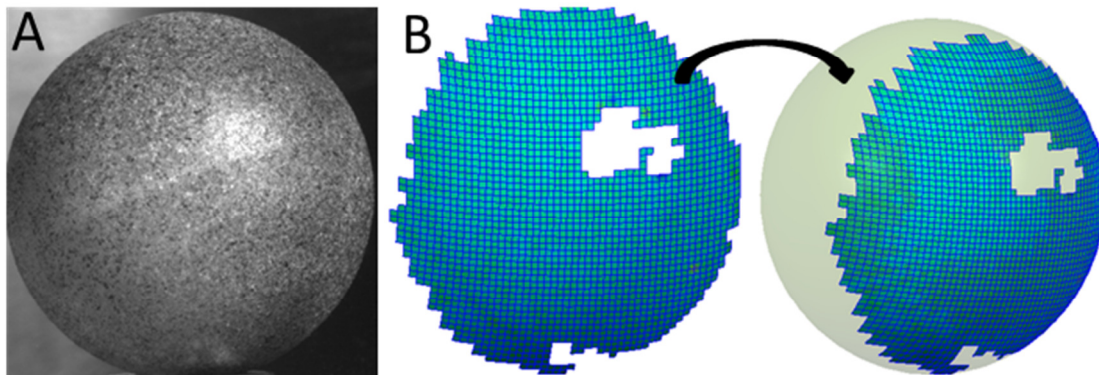
Figure 2-1: Examination of spherical fit for (A) raw left camera image (B) DIC virtual data and application to a spherical fit using the data

Experimental Blister Fixture

The first blister tests on PEMs by Dillard et al. [24] were performed by bonding membranes to ferrules and mounting them into a modified Swagelok® tube fitting. The blister was then pressurized with a syringe pump. This apparatus provided a single blister capable of being tested to failure at multiple pressurization rates. In subsequent studies [27,30] an eight cell fixture connected to multiple pressure transducers and controlled by LabVIEW was used to increase the number of tests performed simultaneously. The fixture and the pressure control system are shown in Figure 2-2 and Figure 2-3. The eight station fixture did not lend itself to DIC measurement because it was metallic and reflective, causing the membrane to be washed out during lighting.
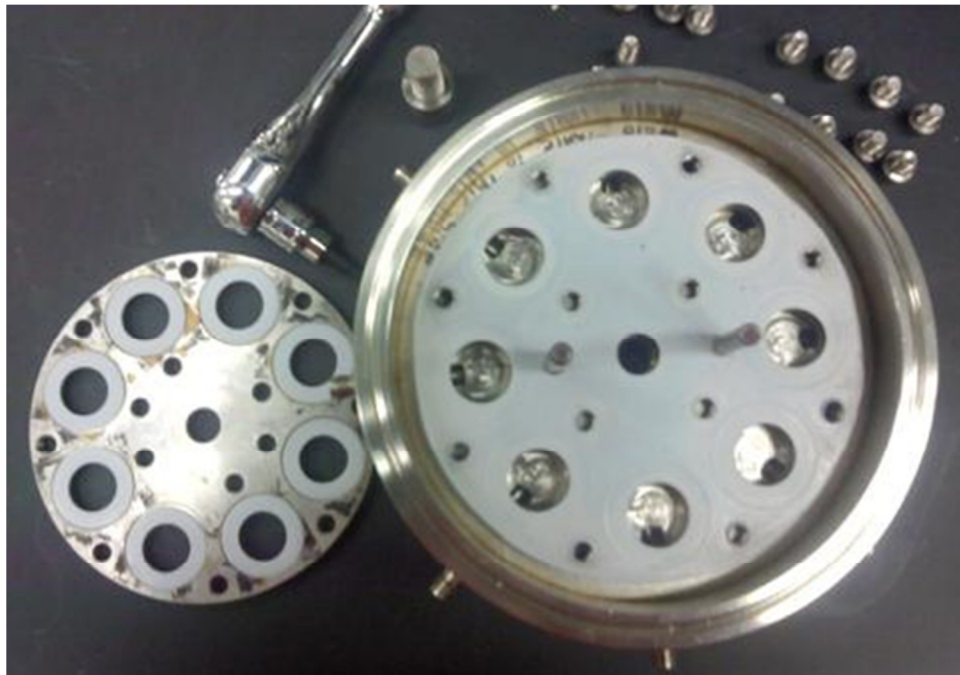
Figure 2-2: Eight station pressurized blister fixture unassembled. Membrane is placed over each hole and mechanically clamped with the top plate
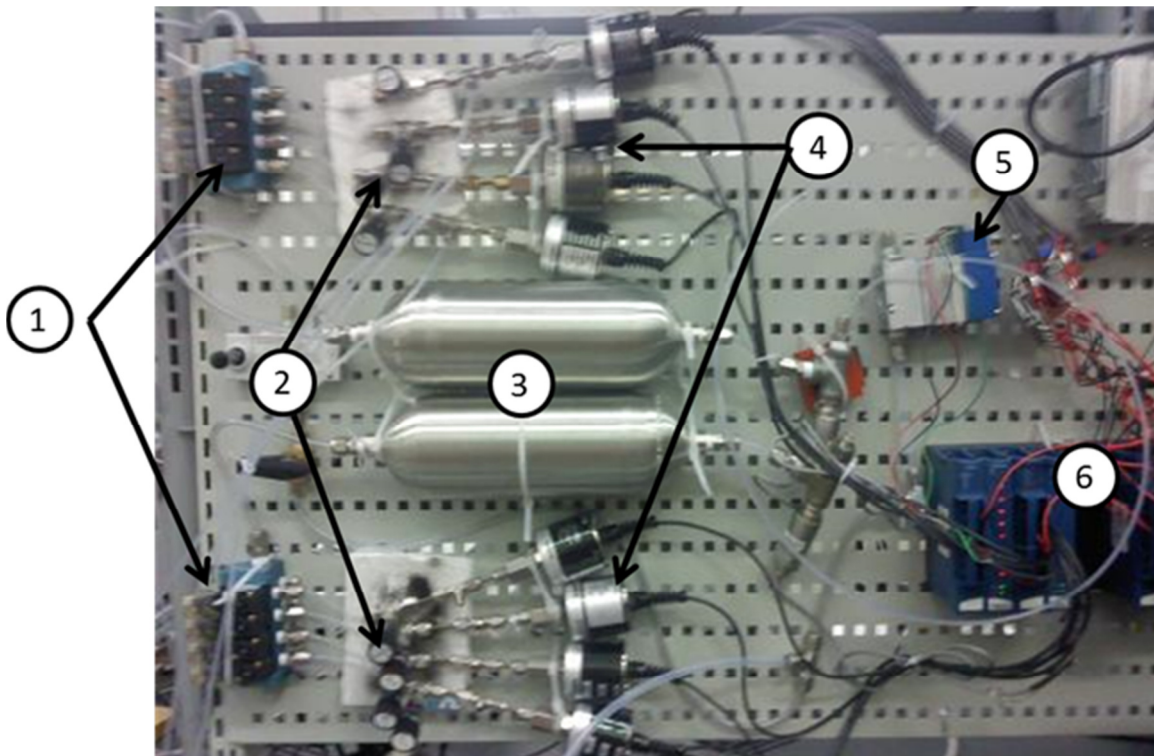
Figure 2-3: Experimental system set up for pressurized blister testing showing (1) cut-off valves, (2) needle valves, (3) system pressure tanks, (4) pressure transducers, (5) pressure regulator, and (6) National Instruments docking station

DIC was first implemented for blister testing of PEMs using the original bonded single ferrule method described previously, with the addition of LabVIEW pressure controls instead of the use of the syringe pump. The membrane was bonded to the ferrule using a basic epoxy and allowed to dry. It was then spray painted with black Krylon® paint to allow DIC capability [30]. A standard desk lamp was used to light the samples from the front. Temperature and humidity were controlled using an environmental chamber with a double pane glass door in the front and an inlet for a humidity control unit in the back. To account for the refraction and reflection from the glass, the DIC was calibrated through the door. The set-up is shown in Figure 2-4. While this method is standard DIC procedure, problems were encountered that were directly related to this procedure.

Figure 2-4: DIC blister fixture with front lighting for testing of PEMs

The first was a clear reduction in lifetime between painted and unpainted samples; the painted samples failed significantly earlier and had more scatter than the unpainted samples. This was thought to be caused by the solvents used in the spray paint and the problem was resolved by switching to Higgins® black India ink for speckling instead. India ink is water based ink and was found to have negligible effect on the pressure lifetime behavior of the membrane. It was airbrushed on in a similar manner to the spray paint application. A comparison of scaled pressure versus lifetime for Gore-Select® series 57 is shown in Figure 2-5, which shows clear improvement for the India ink samples. Pressure is scaled by the relation in the Hencky stress solution at the center of the material, given by Eqn. 2.5.

$$P_{Red} = \frac{B_0}{4}\left[\frac{p \cdot a}{h}\right]^{2/3}$$

2.5

This scaling procedure assumes that the material properties are the same by ignoring the modulus but scales for thickness (*h*) and fixture radius (*a*) differences to account for the difference in fixture radius between the eight station fixture and the DIC ferrule fixture (9.525 mm and 10.3 mm respectively).
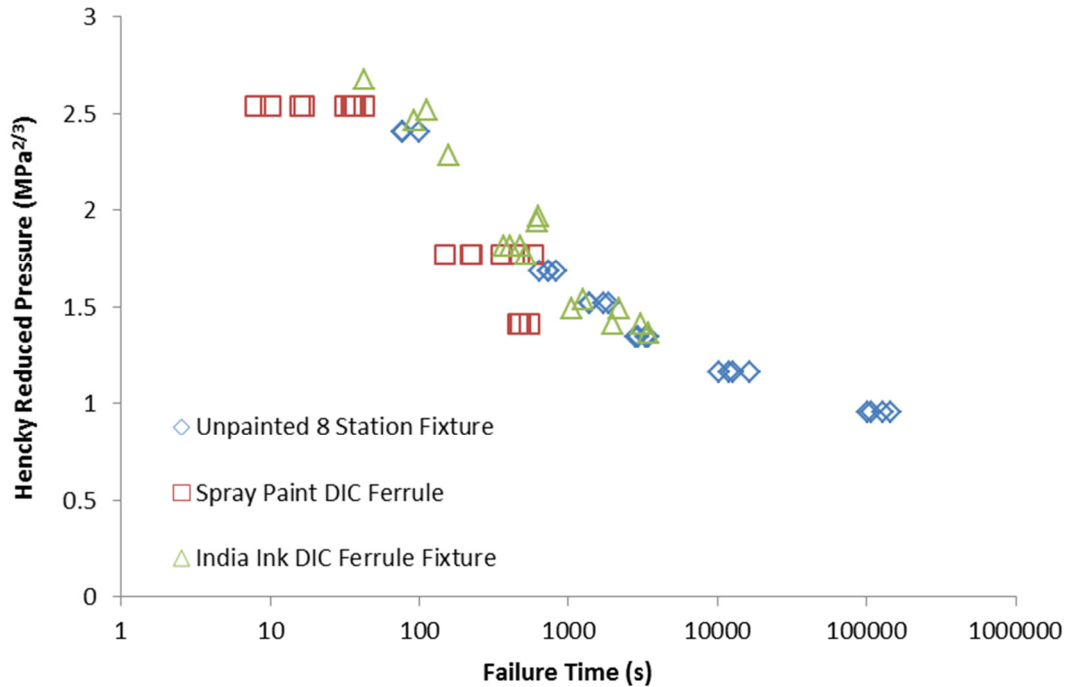
Figure 2-5: Lifetime comparison of spray painted, airbrushed India ink, and unpainted samples for Gore-Select® series 57 PEM under constant pressure loading at 90°C and nominally dry conditions obtained using the eight station fixture from Figure 2-2 (unpainted) and the DIC ferrule (spray paint and India ink)

The second problem encountered was the inability to conduct DIC measurements on transparent membranes, because the use of the DIC requires clear contrast between the background and the speckle pattern, a requirement that was not satisfied when testing a transparent membrane lit from the front. This can be easily seen in Figure 2-6. A further problem was found when testing a material such as Gore-Select® series 57, which is not transparent and therefore can be tested with lighting from the front. However, the appearance of lighting "hotspots" due to the reflection of light off the curved blister surface caused data loss by obscuring the speckle pattern on the membrane, shown in Figure 2-7.
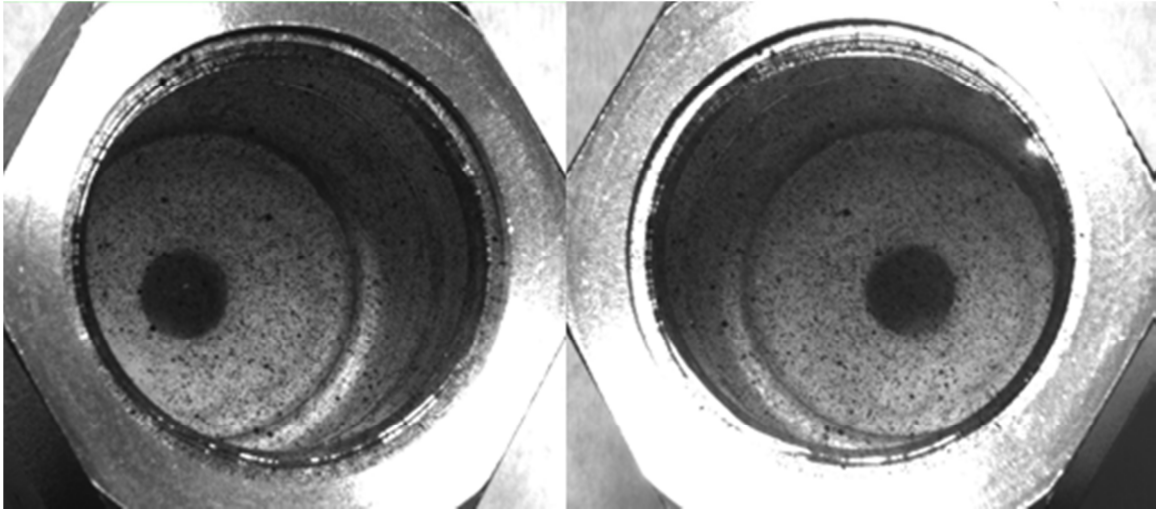
Figure 2-6: Left and right images of NR211 showing transparency and an unclear speckle pattern for the cameras to track
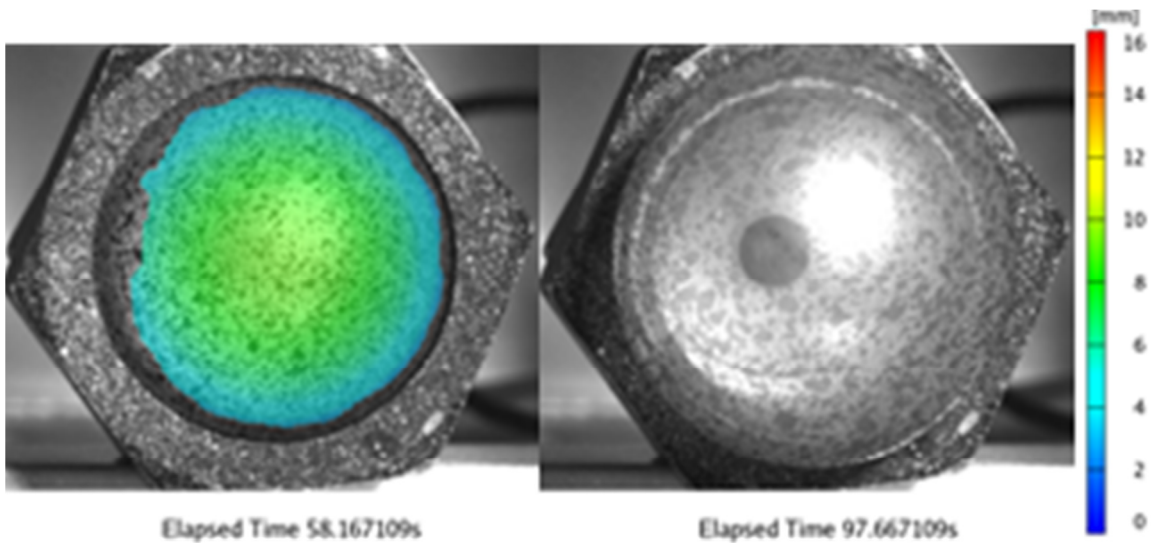
Figure 2-7: Comparison of low curvature and transparency (Left) with an image after further deformation of a highly curved blister with lighting "hotspots" (Right)

To solve the previous issues, a fixture capable of being lit from the back was implemented. This backlighting eliminates the glare caused by reflection off the highly curved surface and allows for easy measurement of both transparent and translucent materials. The backlit DIC blister fixture is a sandblasted polycarbonate fixture developed in two halves that mimics a single cell from the eight station fixture shown in Figure 2-2. The sandblasted polycarbonate acts as a primary light diffuser, and is shown in Figure 2-8.
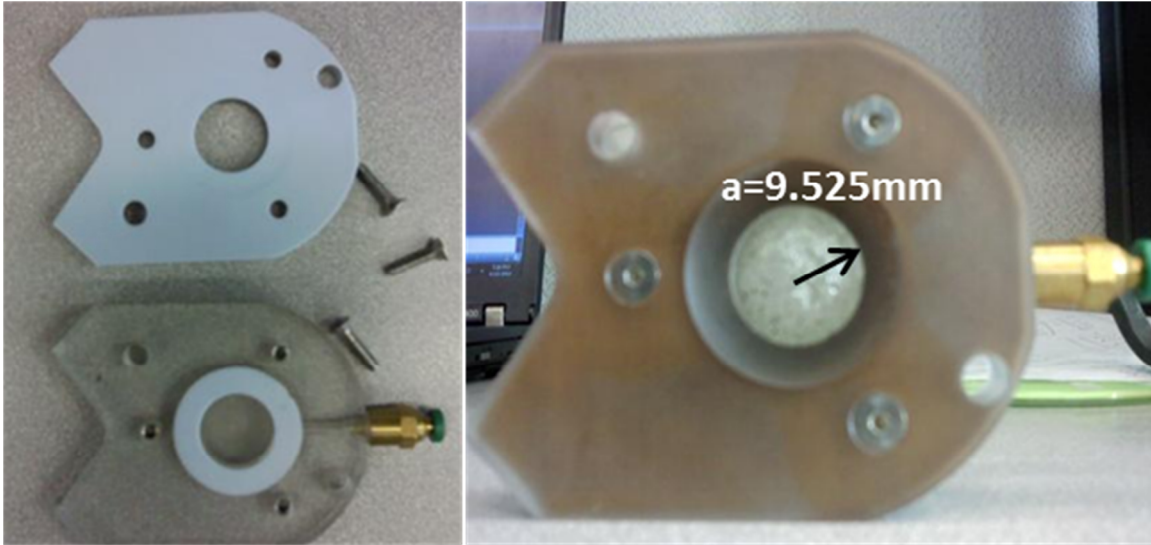
Figure 2-8: DIC fixture shown unassembled (left) and assembled (right)

This fixture has a 9.525 mm orifice radius and is lined with Teflon® in a similar manner to the eight cell fixture. The pressure input is on the side to maintain a homogeneous surface behind the blister for even lighting. Three screws are used to mechanically clamp the membrane. Since no bonding is necessary, the samples are airbrushed with a speckle pattern pre-test and allowed to dry before being placed in the fixture for testing. A small inlet for a fiber optic cable was made in the backside of the environmental chamber. The set-up is very similar to the previous method but does not require front lighting by a desk lamp. It is shown in Figure 2-9. For further light diffusion, a piece of white paper is placed directly behind the fixture to reduce the minor but noticeable variations in lighting caused by the texture of the sand blasted polycarbonate.
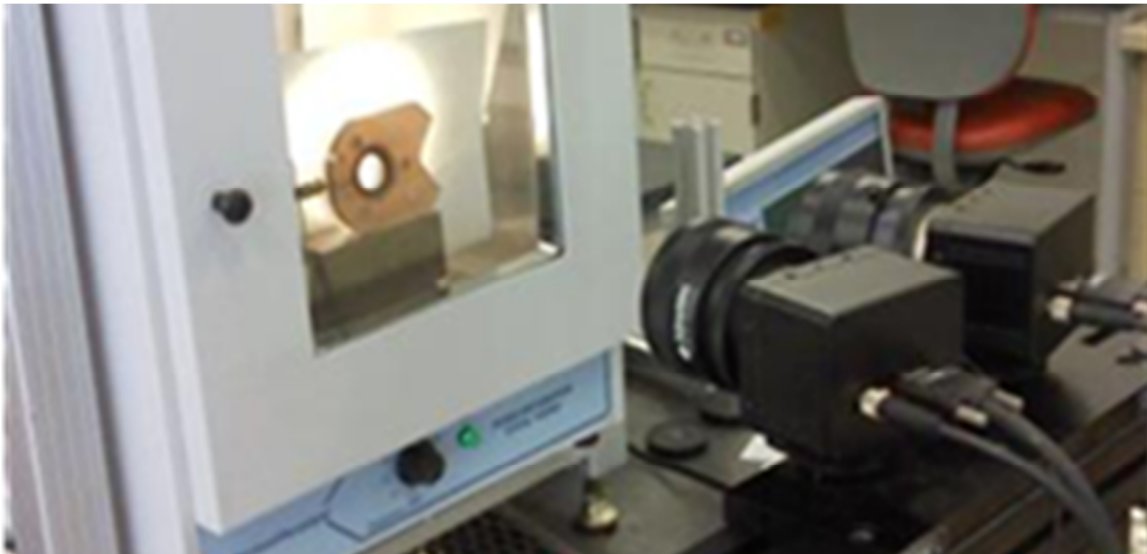
Figure 2-9: DIC blister fixture with backlighting for testing of PEMs

Analysis of Experimental Methods

Nafion® NR211, with a thickness of 25 μm was biaxially tested with a blister test and DIC using ramped pressure at two rates, 0.1 kPa/s and 1.0 kPa/s. This is the blister analog to uniaxial ramp loading. Tests were ramped to failure and the biaxial true stress- true strain curve was analyzed, with true stress calculated using a quasi-static version of Eqn. 2.1 and the assumption of constant volume deformation, which combine to give Eqn. 2.6.

$$\sigma_{true}(t) = \frac{p(t) \cdot R(t)}{2h_0}\lambda_1(t)\lambda_2(t) \qquad\qquad 2.6$$

The radius of curvature was calculated by selecting approximately 450 data points in the central region of the blister and using those data points as the basis of a spherical fit. This selection method was used because the blister is known to be well approximated by a sphere in the equal biaxial central region but becomes less so as the edges are approached. This fitting process is illustrated in Figure 2-10. As the number of data points increases (radially from the center, meaning that more data points means fitting data farther and farther outside of the central region) the radius of curvature measured decreases and the residual increases. At approximately 500 data points this trend begins to plateau, seen in Figure 2-11. Any significant further reduction was found to give inconsistency in the radius measured radius over time, so a value of 450 data points was used for the spherical fit.
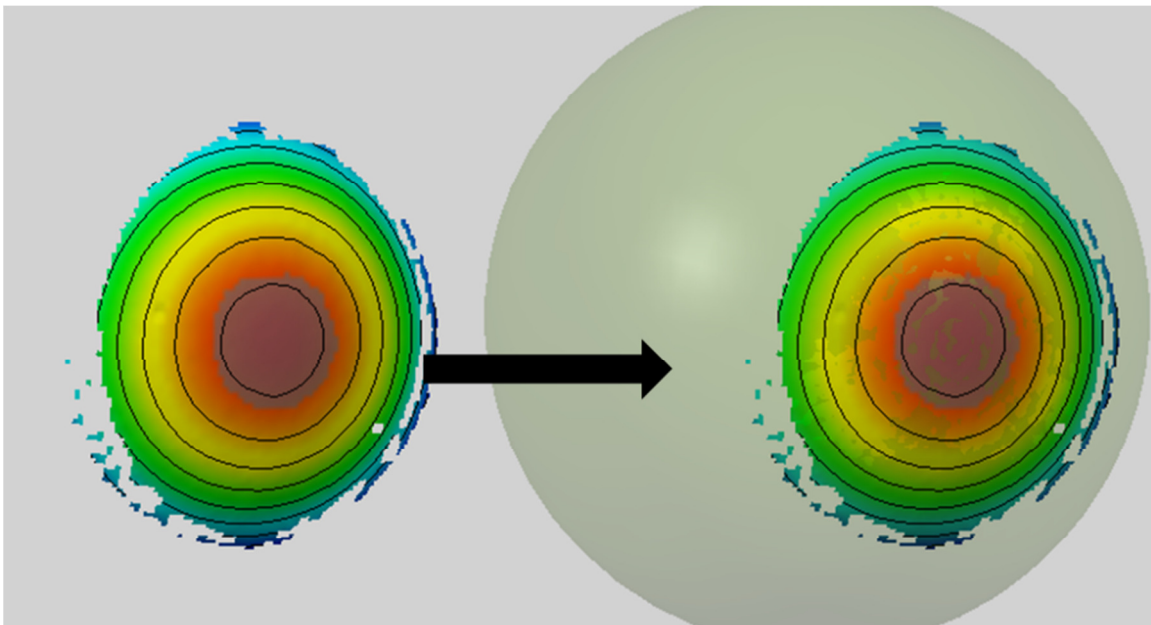
Figure 2-10: Application of spherical fit to the central region of data, approximately 450 data points making up roughly 10% of the total data measured. The contour shows constant values of the Z-coordinate, and the spherical fitting region is highlighted.
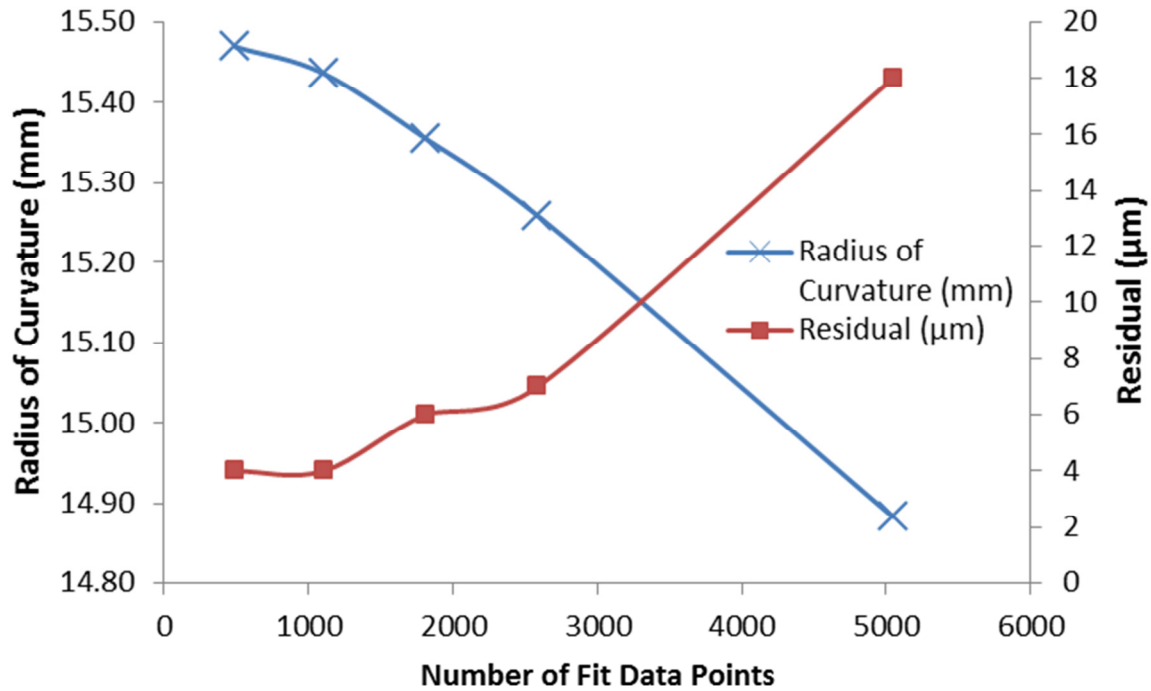
Figure 2-11: Change in measured radius and residual versus the amount of data fit

The extension ratios in the principal directions, denoted as λ, were calculated as discussed previously using the ARAMIS software package. To improve the smoothness of the data and eliminate noise, a median filter was run three times over the data set, operating on a 5x5 matrix of data points. This improvement in the smoothness of data is apparent from the engineering strain contour plots shown in Figure 2-12.
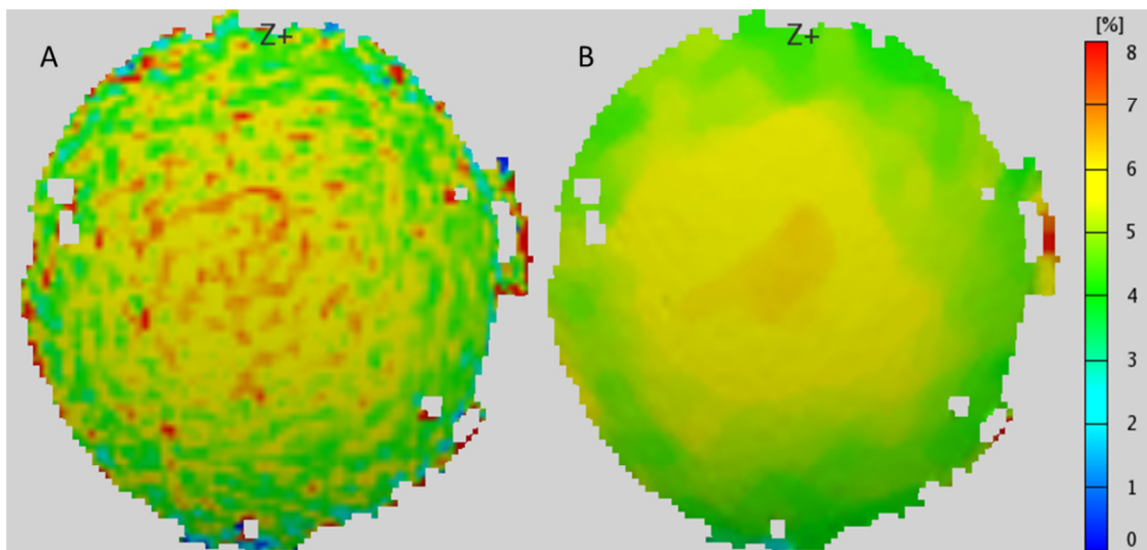
Figure 2-12: Blister test comparison of data (A) before filtering and (B) after filtering

Blister deformation was first assumed to be axisymmetric to compare the deformation to reported linear elastic bulge test data. The axisymmetric assumption was a self-checking

16

procedure; if it were not the data would not collapse onto a satisfactory radius-height curve based on a true center. Figure 2-13 shows that the data does collapse well, implying that the axisymmetric assumption was reasonable.
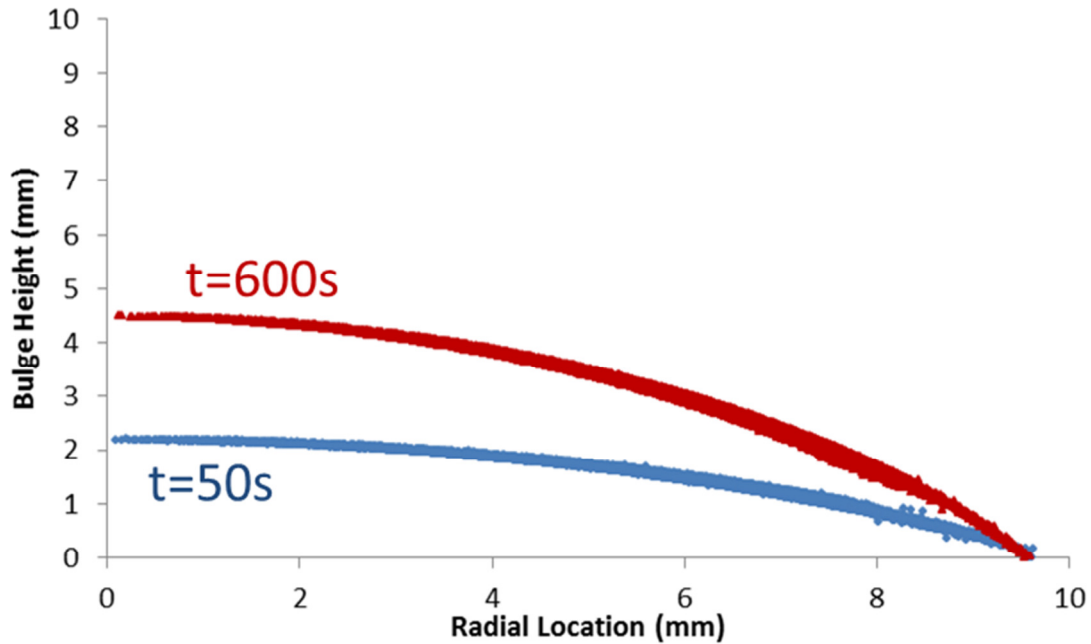
Figure 2-13: Bulge height versus radial position using a single defined center and assuming axi-symmetry around that center

The principal strains at multiple different times can therefore be plotted similarly. This plot is shown in Figure 2-14. Examining this plot shows scatter toward the edges of the blister that is caused by the lack of data surrounding the edge; edge points are therefore inherently noisier. It also shows that the data at small strains (t=50s), perhaps within or very near the linear region, conforms qualitatively well to linear elastic predictions given by Tsakalakos in [38]. Tsakalakos predicts that the radial strain (ε_1) will be approximately constant over the blister, while the circumferential strain (ε_2) will be equivalent at the center and decay to zero at the edge to satisfy the clamped boundary condition. However, at large strains, nonlinearity begins to affect the material and the radial and circumferential strains follow the same shape for much more of the blister.
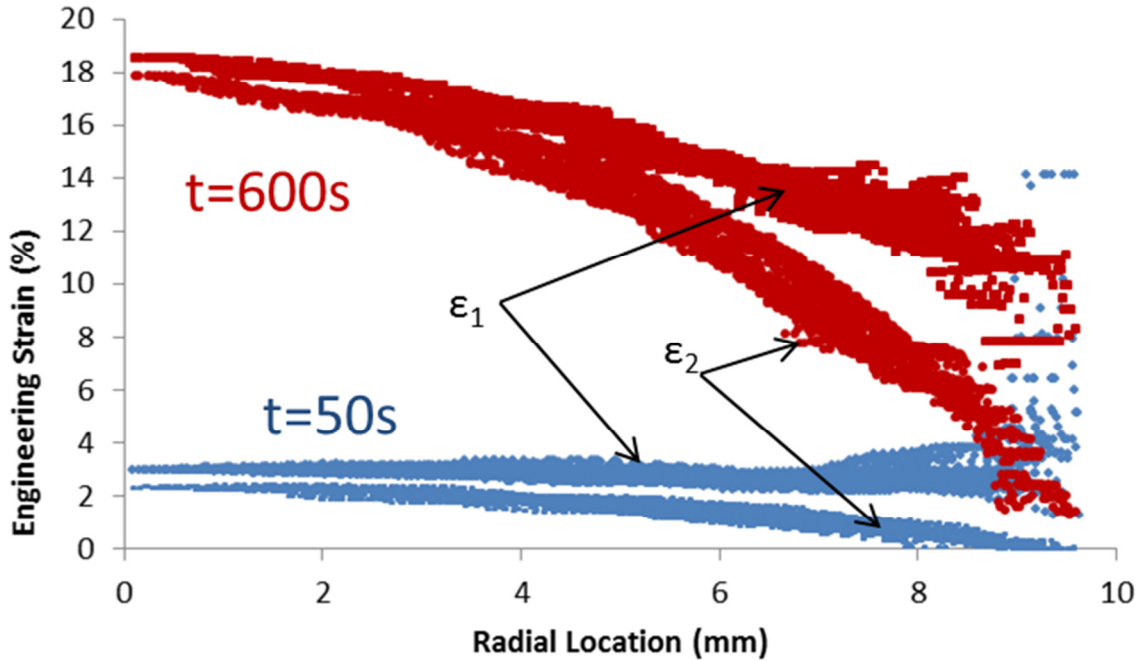
Figure 2-14: Strain distribution in a Nafion® blister test at 50s and 600s showing the major and minor principal directions

Engineering stress, calculated using Eqn. 2.1, versus engineering strain behavior as measured using the blister test was compared to ambient conditions data (25°C and 45% RH) measured by Silberstein et al [15] and was found to show excellent agreement for the lower pressure ramp rate of 0.1 kPa s^{-1} which corresponds to a strain rate on the order of 2×10^{-4} s^{-1}. This rate was not constant since pressure was being controlled and this may contribute to the slight variations from the cruciform data, which was taken under constant displacement of 14 μm s^{-1}. The comparison is shown in Figure 2-15. The yield and the initial modulus agree very well for both tests and increase confidence in the blister method used to measure the stress and strain.
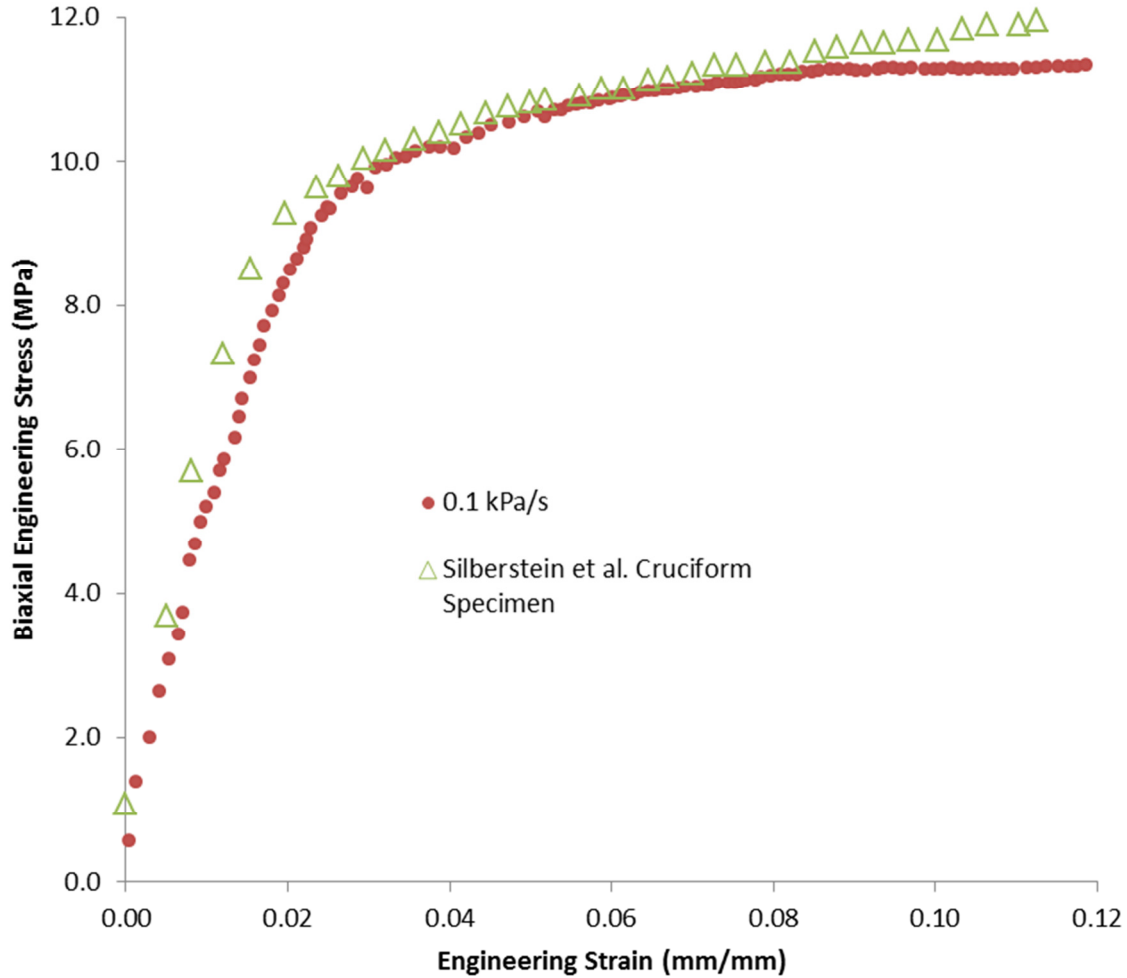
Figure 2-15: Blister test biaxial engineering stress versus engineering strain curve of NR-211 membrane at 0.1kPa/s ramp rate at ambient conditions (25°C and 45% RH) compared with an equal biaxial cruciform test at a displacement rate of 14 μm s^{-1} from [15].

To examine the true stress-true strain behavior between different ramp rates, true strain was calculated using Eqn 2.7.

$$\varepsilon_{true} = \ln(\varepsilon_1 + 1) \qquad\qquad 2.7$$

The strain of interest was at the very center of the bulge in the highest strain region. Using Eqns. 2.6 and 2.7, the stress and strain in this central region were calculated for a given ramped pressure test. Results are shown in Figure 2-16.
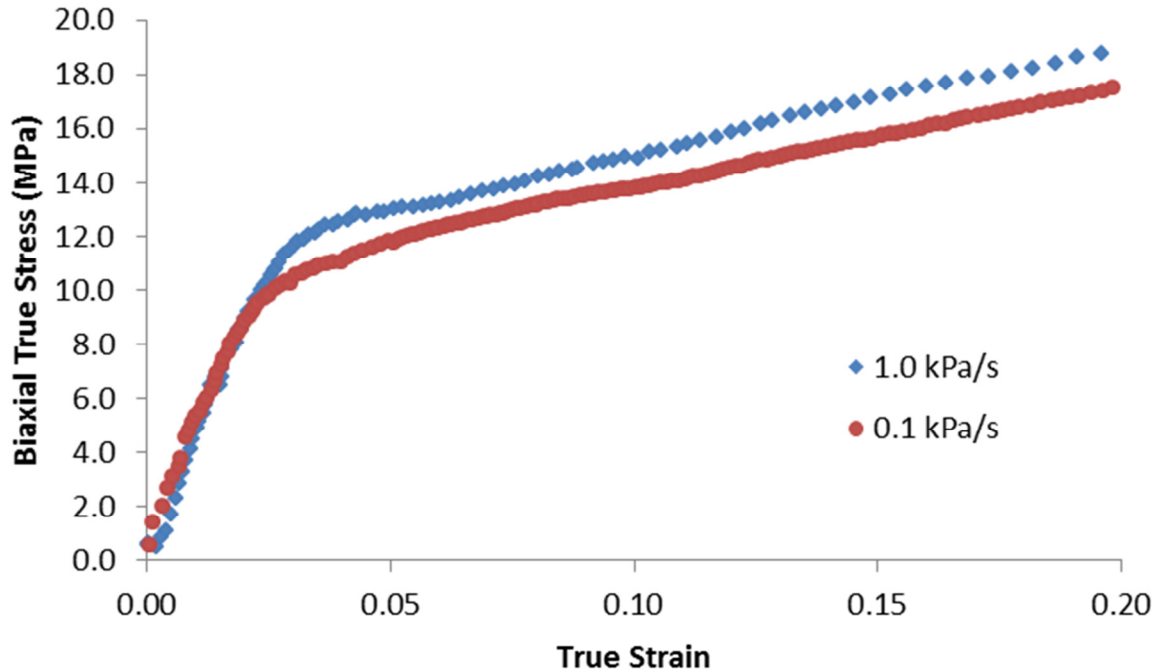
Figure 2-16: Comparison of 1.0 kPa/s and 0.1 kPa/s ramp rates at ambient conditions using blister test

The initial biaxial modulus value shows very slight stiffening at the higher ramp rate as well as an increase in yield strength of the material. The true strain rates before yield were found to be approximately 2×10^{-4} s^{-1} and 1×10^{-3} s^{-1} for the 0.1 and 1.0 kPa/s ramp rates respectively, although they vary slightly due to pressure being controlled instead of displacement.

Conclusions

A method was developed for applying digital image correlation to thin, transparent or translucent proton exchange membranes without affecting the constant pressure lifetime behavior of the material. This enables the measurement of deformation and consequently stress without assuming a material model. Nafion® was found to deform axi-symmetrically and the central region was found to fit well to the spherical approximation made.

Using a spherical fit, the biaxial engineering stress and engineering strain of Nafion® NR-211 was measured and compared to Silberstein et al. [15] with good agreement, despite the inability to control strain rate directly. Using the assumption of constant volume deformation (Poisson's ratio of 0.5), which is a good approximation after yield, the true stress and true strain curves of 0.1 kPa/s and 1.0 kPa/s were compared to each other. Although there is less control over the strain rate in the blister test, the rate of applied pressure may be controlled to examine rate dependence.

Future work with the DIC of blisters will attempt to extend the measurements further into the realm of material failure under biaxial loading as well as the determination of modulus, Poisson's ratio, and yield behavior under biaxial loading. Since DIC measurements are full field, no assumptions on geometry must be made (although they can for simplification), such as constant curvature or small deformation. Perhaps most importantly it captures irregularities in

deformation, including principal strain directions and magnitudes. This makes it an invaluable tool for observing strain localization that lead to leaking in a PEM.

Acknowledgements

Chapter 3: Stress-Lifetime Characterization of Proton Exchange Membrane Using 3-D Digital Image Correlation and Pressure-Loaded Blister Tests

Abstract

The strength of the proton exchange membrane (PEM) and its ability to withstand cyclic, environmentally induced stresses plays an important role in membrane integrity and consequently, fuel cell durability. In this study, pressure loaded blister tests are used to characterize the biaxial strength of a model commercially available membrane, Gore-Select® series 57, at the 90°C dry condition under ramped, constant and cyclic pressure loading. Gas leakage is used as the failure criterion, making it analogous to the stresses and failures seen during fuel cell operation. Three-dimensional digital image correlation is used to measure the deformation of the bulging membrane. A quasi-static, spherical pressure vessel approximation of the central portion of the blister then allows the biaxial stress state at this location of the PEM to be tracked through time. A damage accumulation model is applied to the data taken during constant pressure loading to determine the damage parameters. The model is then used to predict the failure of blisters from ramped and cyclic fatigue test modes. The successful lifetime prediction suggests an understanding of the stress state in the blister test and the model's ability to relate different mechanical loadings and predict failure.

Introduction

Characterization of the mechanical strength and degradation of the proton exchange membrane (PEM) is an important step to improving overall fuel cell longevity. Mechanical failure of the PEM, specifically the formation of pinholes due to the cyclic nature of the fuel cell environment (i.e. cyclic temperature and humidity changes), have been found to be an important factor in gas crossover and ultimately cell inefficiency. These pinholes are formed by induced stresses in the membrane from hygrothermal expansion under biaxial constraint between the rigid flow channels [6,39]. Since the constraint is biaxial, the environmentally induced stresses are also biaxial. Blister (or bulge) testing has been used extensively in the evaluation of thin films in a biaxial stress state. In past research, Dillard et al. have used the blister test to provide an ex-situ PEM strength characterization that considers gas leakage as the failure criterion as opposed to uniaxial tensile rupture [24,25,27,31]. In these studies, Hencky's linear elastic solution for a circular film under pressure provides an analytical guide to approximate stresses in the blister [28]. However, these approximations are based on linear constitutive theory while PEM behavior is known to show some nonlinearity at high strains.

One goal of this study is to experimentally measure the stress state in the blister, particularly in the central portion where the maximum stress and failure occurs. Because of the axial symmetry of a circular blister, this central region is under equal biaxial stress, which can be determined using spherical pressure vessel theory given in [40], where *p* is pressure, *R* is the radius of curvature, and *h* is the membrane thickness.

$$\sigma_1(t) = \sigma_2(t) = \frac{p(t) \cdot R(t)}{2h(t)} \qquad\qquad 3.1$$

Eqn. 3.1 is based on quasi-static force equilibrium and does not require knowing the constitutive properties of the membrane. The value of R was determined at each instant of time using the computer vision-based digital image correlation (DIC) method. DIC has been used with success to measure full-field deformation in multiple engineering disciplines [35,36,41]. In the blister test, R was calculated by fitting a sphere to the DIC-measured deformation data set using a least squares approach. Figure 3-1 illustrates this fitting concept and Table 3-1 gives the fit statistics for three different time periods, recognizing that they are a representation of the blister evolution over a single experiment. It should be noted that the maximum and minimum deviation give a range of error that incorporates outliers, while the residual provides a baseline deviation of the experimental data from the spherical fit.
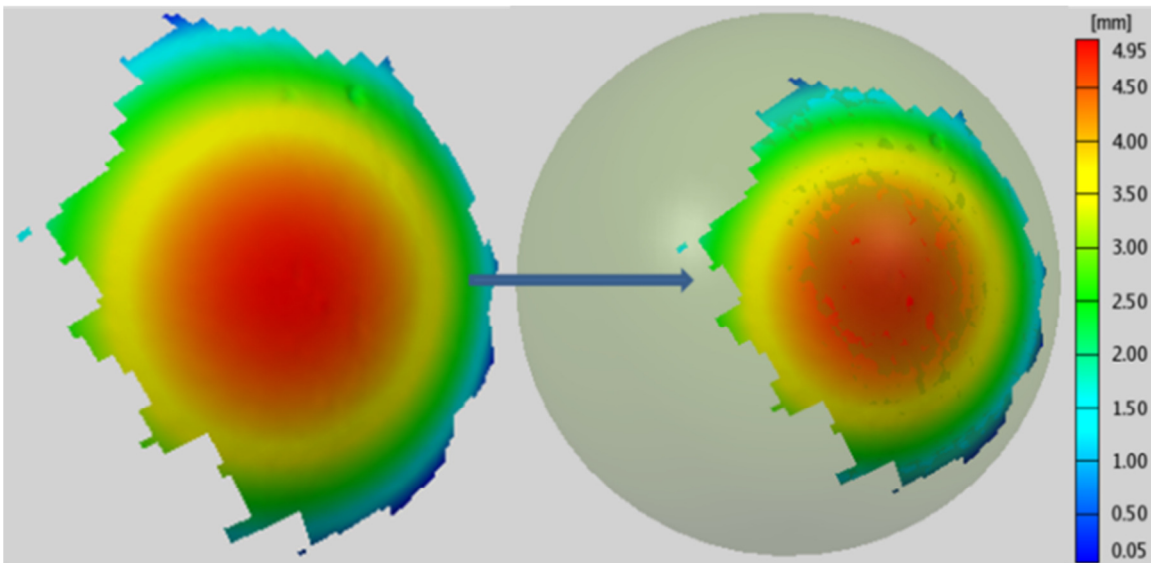
Figure 3-1: Fit of blister model to sphere using a least squares approach to a constant pressure test of Gore-Select® series 57 membrane tested at 90°C and nominally dry conditions

Table 3-1: Sphere fitting statistics for constant pressure test at 0.5s, 50s, and 400s

Statistics: Spherical Fit to Blister Data			
	0.5s	50s	400s
Radius (mm)	18.158	11.764	9.815
Min Deviation (mm)	-0.200	-0.222	-0.047
Max Deviation (mm)	0.223	0.039	0.080
Standard Deviation (mm)	0.016	0.016	0.010
Residual (mm)	0.011	0.011	0.007

The second goal of this study was to establish damage parameters and make stress-lifetime predictions. Given the stress histories during blister tests, stress-lifetime curves may be

23

established based on constant pressure tests and the assumptions of a power law equation and linear damage accumulation. The same power law equation can then be used to predict the lifetime of the membrane under ramped and fatigue blister loading which can be compared with experimental failure results, and in the future potentially hygrothermal stress histories seen in fuel cell operations.

Experimental Procedure

The procedure for pressure-loaded blister testing of PEMs has been described in detail in previous works [24,25,31,27]. The use of the DIC requires slight modification of the method, which will be shown here. The fixture used is polycarbonate with a 9.525 mm radius opening and Teflon® lining in the region around the opening that constrains the PEM. The sand blasted polycarbonate fixture allows for diffused backlighting of the transparent PEM specimen and the Teflon® reduces membrane damage at the clamped edge. The fixture is shown in Figure 3-2. Testing of the Gore-Select® series 57 PEM was performed at 90°C and uncontrolled humidity that was measured to be <1% relative humidity. Three separate test procedures were run:

1. Constant pressure was used to fit material stress-life parameters
2. Ramped pressure was used to validate the damage parameters under a different loading profile
3. Fatigue pressure at multiple duty cycle ratios was used to evaluate the extent to which the model applies under cyclic stress histories
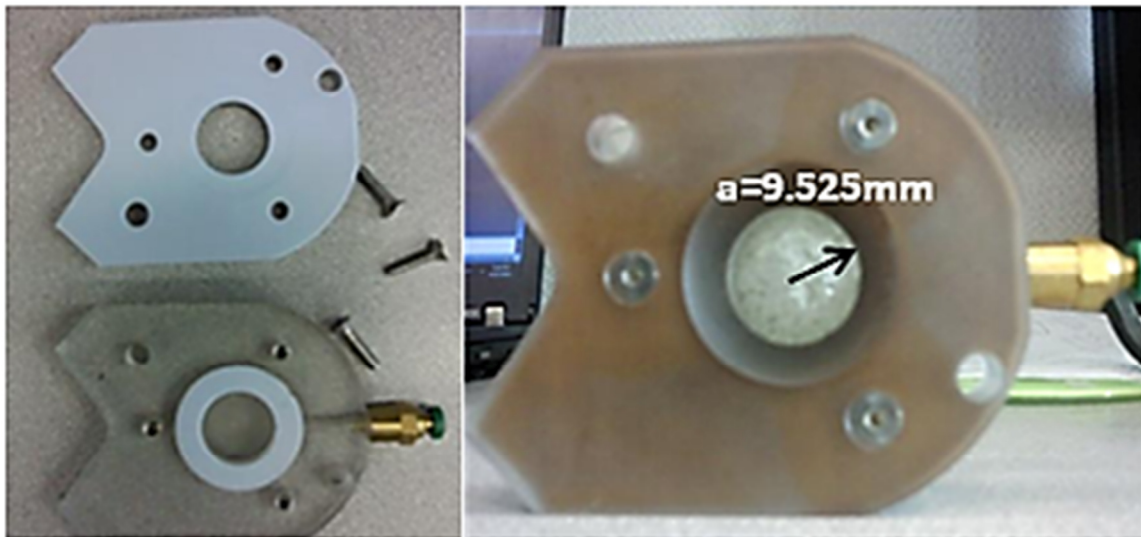
Figure 3-2: Unassembled (Left) and assembled (Right) blister fixture for use with the DIC

The extent of testing completed with the DIC is summarized in Table 3-2.

24

Table 3-2: Summary of blister testing performed with the DIC

Constant Pressure	Ramp Pressure	Fatigue Pressure	
Pressure	Rate	Duty Cycle (Load:Relax)	Pressure
19.25 kPa	1.0 kPa/s	10s:4s	9.3 kPa
19.23 kPa	0.5 kPa/s	10s:4s	9.3 kPa
23.10 kPa	0.1 kPa/s	10s:10s	9.2 kPa
15.21 kPa		4s:10s	9.2 kPa
11.27 kPa			
7.23 kPa			
6.75 kPa			
4.45 kPa			

The DIC system used is the GOM ARAMIS v6 software provided through Trilion Corporation. Schneider-Kreuznach cameras were used with 50 mm lenses for all the testing. Aramis reports measurement capability of displacement out-of-plane to an accuracy of 3×10^{-5} times the field of view (25 mm × 20 mm). This field of view therefore corresponds to measurement accuracy on the order of 1 micron. The DIC method requires application of a random speckle pattern to the surface of the membrane before testing. Higgins® India ink is applied lightly with an airbrush to each sample individually (shown to the left of Figure 3-3); this ensures the pattern is non-repetitive and able to be tracked. Commercial spray paint is typically used in many DIC applications but often contains organic solvents like acetone or toluene which can affect the mechanical integrity of the thin PEM (18 micron). India ink does not have such solvents and therefore avoids those issues. The experimental set-up is shown to the right in Figure 3-3. It includes a fiber optic light source, a light diffuser, and the polycarbonate fixture inside an oven with a double pane glass door for the DIC cameras to photograph through. To maintain accuracy, the DIC is calibrated through the glass with a calibration deviation (deviation of left and right camera) between 0.04 and 0.05 pixels. The cameras were positioned approximately 15 cm apart and 45 cm away from the specimen with an angle between cameras of approximately 20°. Images were taken for ramped pressure tests at 1 frame per second over the lifetime of the test. For constant pressure, 2 frames per second were taken for the first 10 seconds, then 1 frame per second for 100 seconds, and on a log decrement for the remaining time. A similar imaging procedure was used for the cyclic data, where the first 10 cycles were completely captured at one frame per second and the following cycles were captured on a log decrement that was based on cycle number; i.e. every 10th cycle was captured at 1 frame per second, then every 100th cycle, etc.
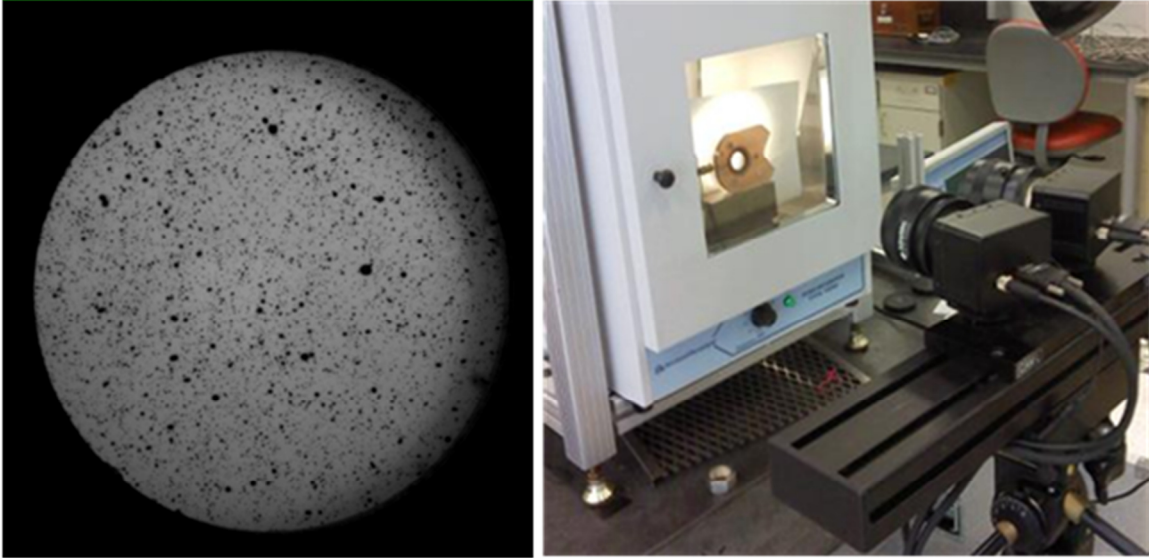
Figure 3-3: Sample stochastic pattern (Left) and blister fixture set-up (right)

Analysis and results

The first pair of images taken of the material in the unpressurized state immediately preceding testing served as the reference state. The radius of curvature was then calculated by fitting a sphere to the data in each image, with each image corresponding to an instant in time. Using Eqn. 3.1 and the known initial thickness of the material (18 µm), the engineering stress was calculated. To reduce any numerical deviations caused by the ARAMIS deformation calculations, the principal strain was taken as the average value over the central, equal biaxial region. Using these strains, the engineering stress was converted to true stress with the isochoric assumption given by Eqn. 3.2. Eqn. 3.3 was then used to convert engineering stress to true stress by taking into account the thickness reduction. λ_1 and λ_2 are the measured principal stretches tangent to the deformed surface, and λ_3 is the stretch normal to the surface.

$$\lambda_1 \lambda_2 \lambda_3 = 1 \qquad\qquad 3.2$$

$$\sigma_{true} = \sigma_{eng} \frac{1}{\lambda_3} \qquad\qquad 3.3$$

Figure 3 shows the reduced data from a single constant pressure test that was used in the model creation, focusing solely on the central region of the blister where failure is seen to occur and the stresses are equal biaxial.
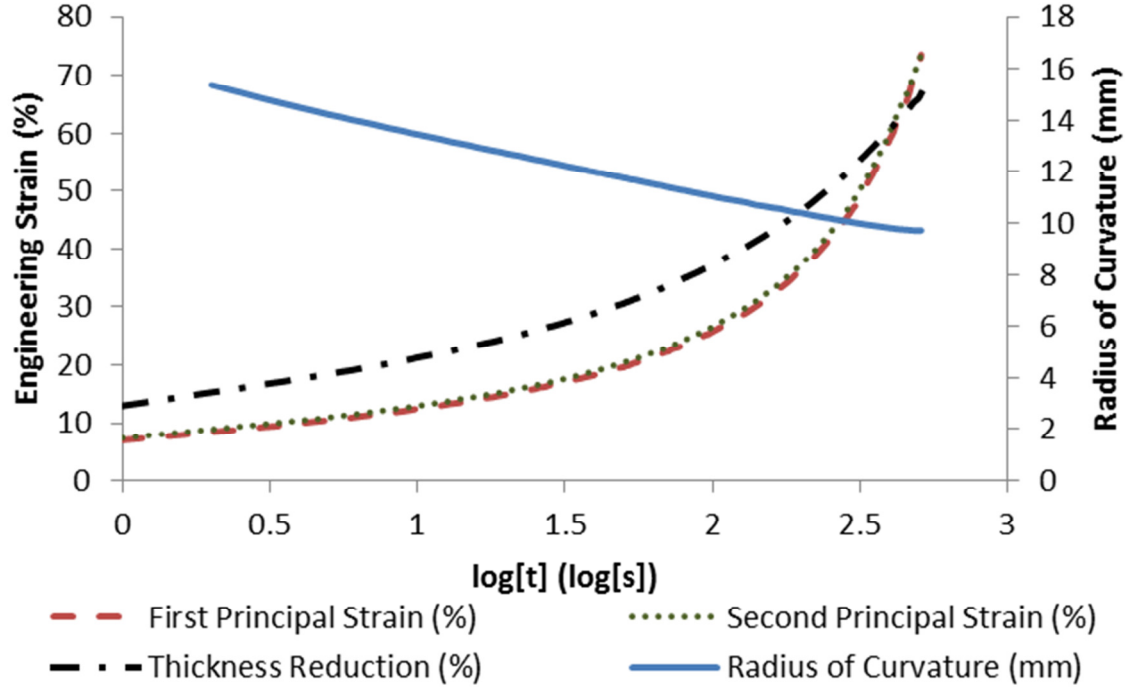
Figure 3-4: Measurements of the central region of the blister throughout the lifetime of a singly blister test. The radius and strain in the center are shown as well as the thickness reduction assuming constant volume deformation.

The damage model used is analogous to the Palmgren-Miner rule for variable amplitude loading which states that failure occurs when

$$\sum \frac{n_i}{N_{fi}} = 1$$

3.4

where n_i is the number of cycles under the ith load and N_{fi} is the number of cycles at the ith load required to fail a material [42]. The extension of this approach to time-dependent failure is given by

$$\int_0^{t_f} \frac{dt}{f(\sigma)} = 1$$

3.5

where $f(\sigma)$ is the instantaneous value of the time-to-failure at a stress σ. This type of linear damage accumulation model has a long history of being used to represent the stress-life behavior of a material under non-constant loading (see, for instance, [43]). However, it is important to recognize that damage accumulates linearly with time and is independent of the order in which load is applied to the material [42]. For this model, the stress-failure time function is assumed to fit a power law, which is a standard damage accumulation assumption.

$$f(\sigma) = A\sigma^B = t_f$$

3.6

27

The lifetime prediction model based on linear damage accumulation is formed by combining Eqns. 3.5 & 3.6 to form Eqn 3.7.

$$\int_0^{t_f} \frac{dt}{A[\sigma(t)]^B} = 1 \qquad\qquad 3.7$$

A and B are material stress-life parameters, and they can be calculated by assuming Eqn. 3.7 holds and fitting experimental data while iterating A and B. The first step to this process was to take constant pressure data and calculate stress profiles to failure for each. Data loss is common with the DIC at large deformations with thin, translucent materials. At times this left gaps between the failure time and the last data point taken. To remedy this, an exponential function was fit to the last 10% of true stress data points calculated by Eqn. 3.3, and the data was then extrapolated to failure as shown in Figure 3-5.
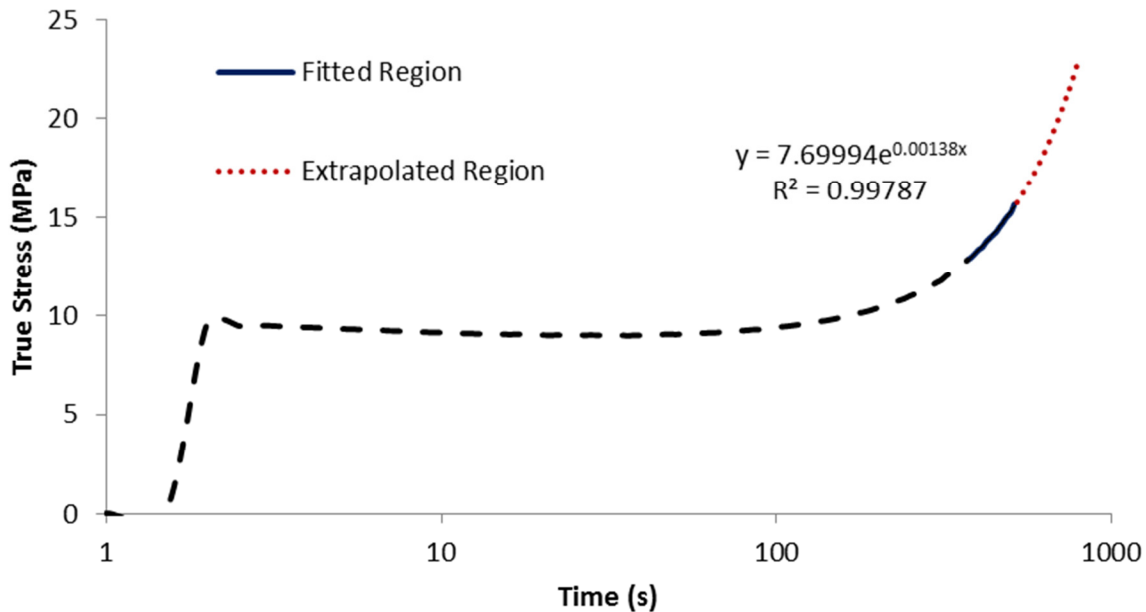
Figure 3-5: True stress profile corresponding to a single constant pressure test.

The sensitivity to the type of extrapolation was evaluated to increase confidence in the extrapolation method and it was found that predictions were insignificantly changed based on the extrapolation profile used, justifying the technique as a valid method to extend stress data (See Appendix F). Using the stress profiles from DIC testing, which can be found in Figure A 1 in Appendix A, and Eqn. 3.5, damage parameters A and B were found by minimizing the error between the predicted failure times and the experimental failure times for the constant pressure data taken. Since wide time ranges were used in the fitting process, the weighted error was based on the squared difference in the base 10 logarithm of time, shown in Eqn. 3.8.

$$(diff)^2 = \left[\log_{10} tf_{exp} - \log_{10} tf_{pred}\right]^2 \qquad\qquad 3.8$$

Values for A and B were calculated to be 4.44×10^8 and -4.85 respectively for units of stress in MPa and time in seconds. Figure 3-6 shows the experimental data and the fitted data based on these A and B values, which lie nearly on top of each other. This is expected, as the predictions from the LDA model in this figure are plotted in comparison to the data used to develop the model. However, it does show consistency of the model and its ability to deal with multiple different pressure loadings and failure times.
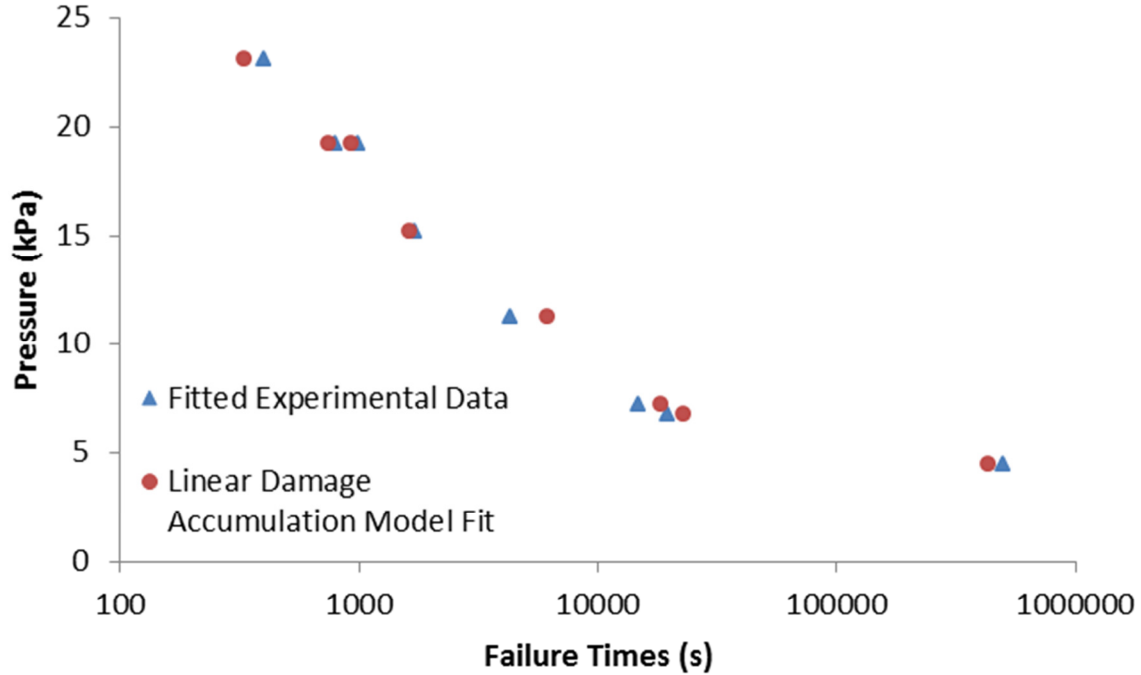
Figure 3-6: Pressure to failure data that compares the LDA fit to the experimental data that is used to create the fit

The second loading method applied was ramp-to-rupture, where the pressure is ramped at a set rate until the blister fails. Again the deformation is tracked by the DIC, and from Eqns. 3.1 & 3.3, the stress profile can be calculated over the lifetime of the blister test. The stress profiles can be seen in Appendix A, Figure A 2. In order to extrapolate stress data to failure, an identical procedure to the one used in the constant pressure method was implemented. Figure 3-7 & Figure 3-8 show a typical pressure profile and stress profile during ramped pressure testing to rupture.

29
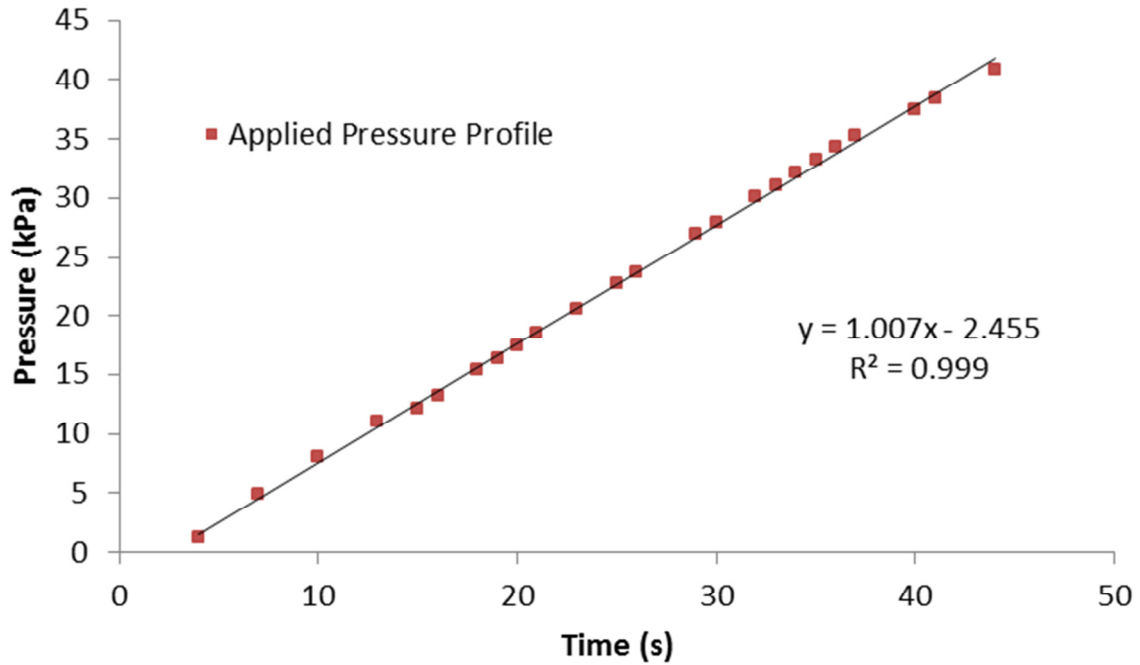
Figure 3-7: Pressure profile for a given ramp to failure test at 1kpa/s
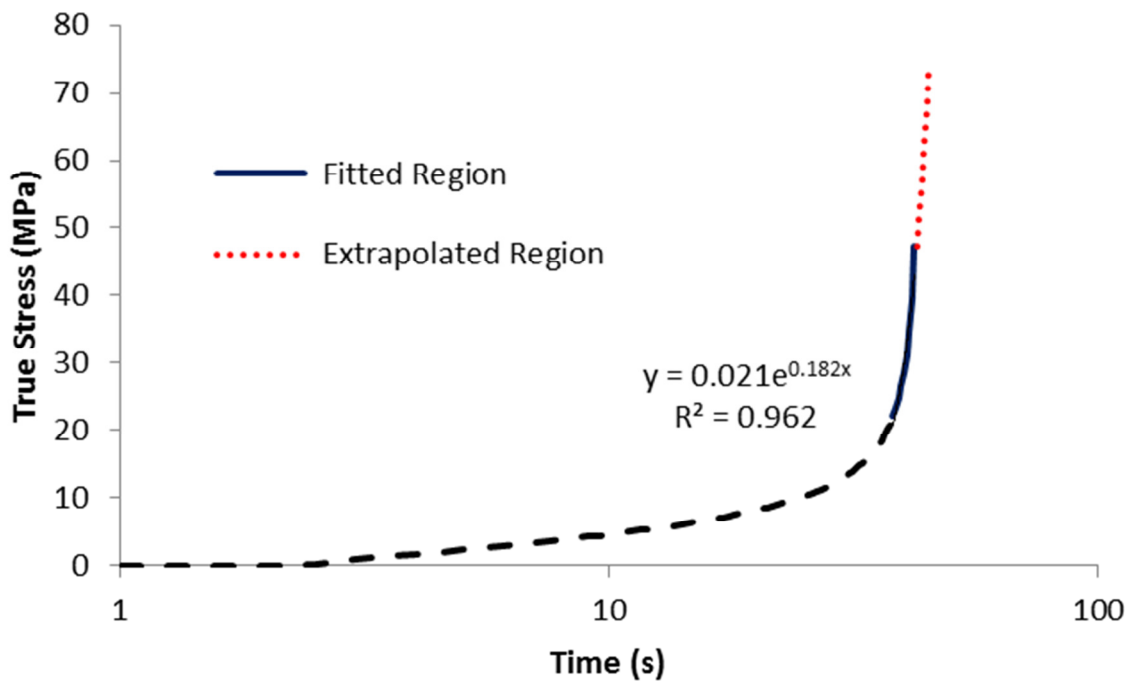
Figure 3-8: DIC stress profile for a ramp to failure test showing very high burst strengths when compared to the constant pressure testing

The third loading method used was fatigue loading at three separate duty cycles (given as load-unload in seconds: 10-4, 4-10, 10-10). Each duty cycle shows different failure time behavior, with the 10-4 failing at the least number of cycles and the 4-10 failing at the most. This can be expected as the time under load varies for each duty cycle. Figure 3-9 shows the pressure

profile of a 10-4 duty cycle test at 9.3 kPa. The applied pressure is nominally zero during the recovery cycle and damage was assumed to not accumulate. The raw stress data can be seen in Appendix A, Figure A 3.
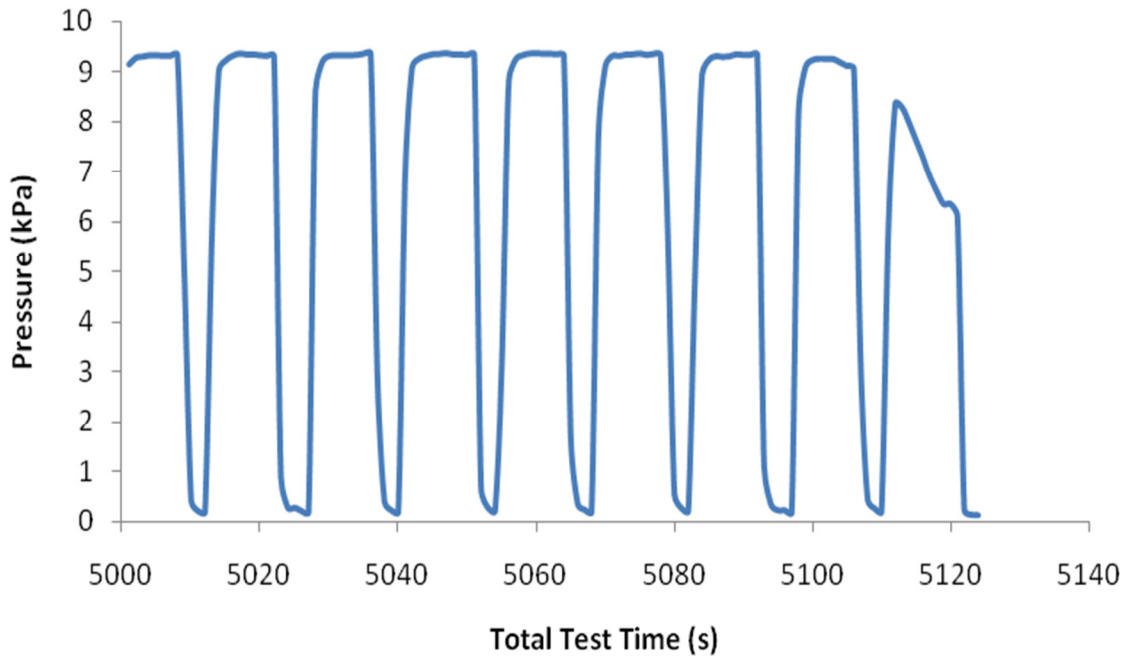
Figure 3-9: Typical fatigue pressure profile showing the onset of failure at approximately 5120s

Figure 3-10 plots the stress during the loading phase and shows an exponential fit to the all the data that is taken after the first 10 cycles.

$y = 3.98893e^{0.00017x}$
$R^2 = 0.99708$
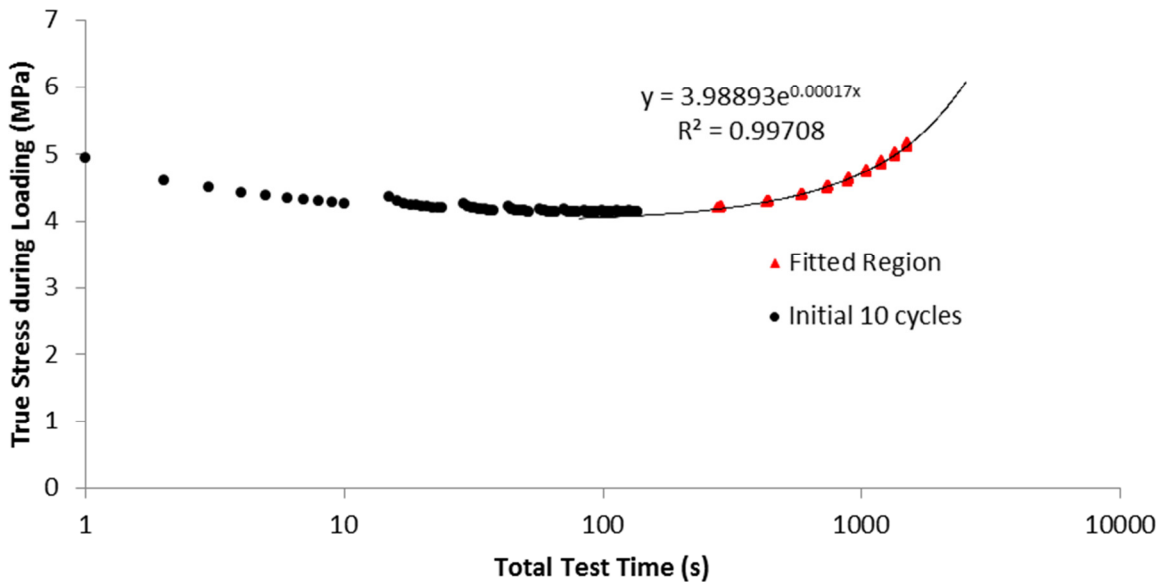
Figure 3-10: True stress during the loading phase of a 10-4 duty cycle

This fit is necessary in order to interpolate the stress between the measured cycles and extrapolate the stresses to failure. The figure only plots the stress during pressurization, as it is assumed that no stress accumulates during the recovery phase.

As the figure shows, the stress in the material changes significantly over a single cycle for the first few cycles (for example, compare the stress at 1s to the stress at 10s, which shows approximately a 15% decrease in stress during the first cycle), but at longer times the stress remains nearly constant over a single cycle and the data points become indistinguishable because of the logarithmic plot, so that the 10 data points taken during each cycle appear as only one (seen in the fitted region). This is better illustrated in Figure 3-11 by comparing the stress evolution in the first cycle to the stress evolution of the 20th and 100th cycles. It is also apparent that, as the membrane undergoes multiple cycles, the stresses begin to increase over time from one cycle to the next (although stress remains approximately constant during a given cycle). This increase from one cycle to the next was fit by an exponential curve, as is shown in Figure 3-10.
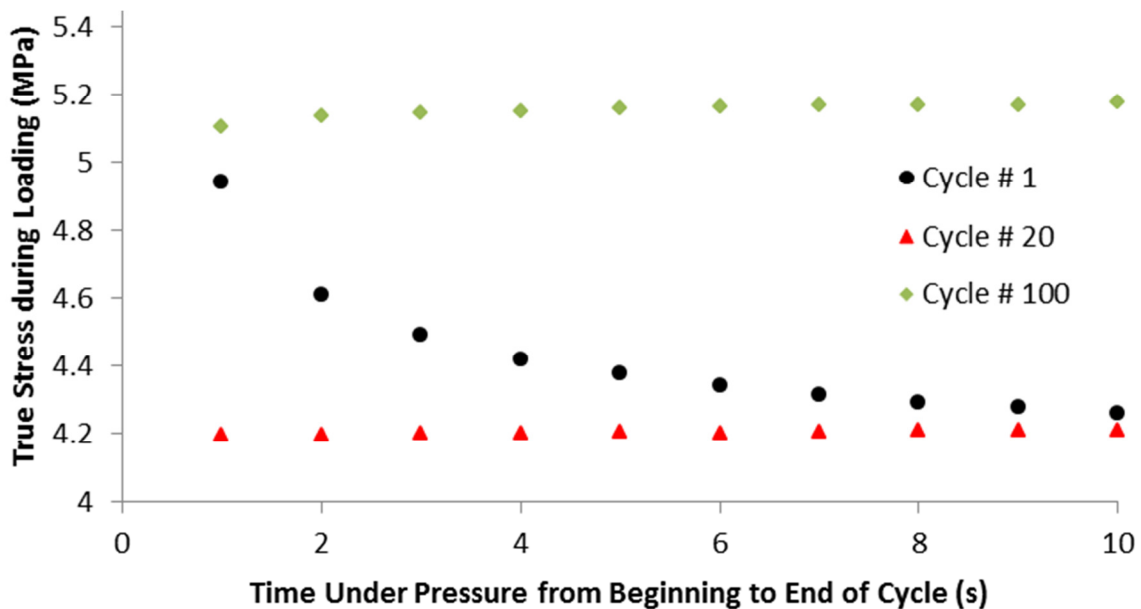
Figure 3-11: Evolution of true stress over chosen cycles. This shows that given a single cycle, by cycle 20 the stress during that cycle is approximately constant and can be simplified as such.

Using the stress profiles measured from the DIC deformation and the damage parameters A and B, calculated from the constant pressure testing, blister failure time predictions were made for each individual test using Eqn. 3.5. Table 3-3 and Figure 3-12 summarize the predictions for each blister test performed.

Table 3-3: Experimental and predicted/fitted failure times for blister tests under multiple loadings

Loading	Pressure	Time Under Load (s)	
		Predicted	Experimental
Constant Pressure	19.25 kPa	748	790
	19.23 kPa	923	990
	23.10 kPa	330	400
	15.21 kPa	1638	1720
	11.27 kPa	6105	4315
	7.23 kPa	18441	14870
	6.75 kPa	22724	19670
	4.45 kPa	431752	493670
Ramped Pressure	1 kPa/s	44	45
	0.5 kPa/s	78	80
	0.1 kPa/s	311	317
10s:4s	9.30 kPa	5650	3650
	9.30 kPa	11850	3270
10s:10s	9.20 kPa	10370	8350
4s:10s	9.20 kPa	17568	10280
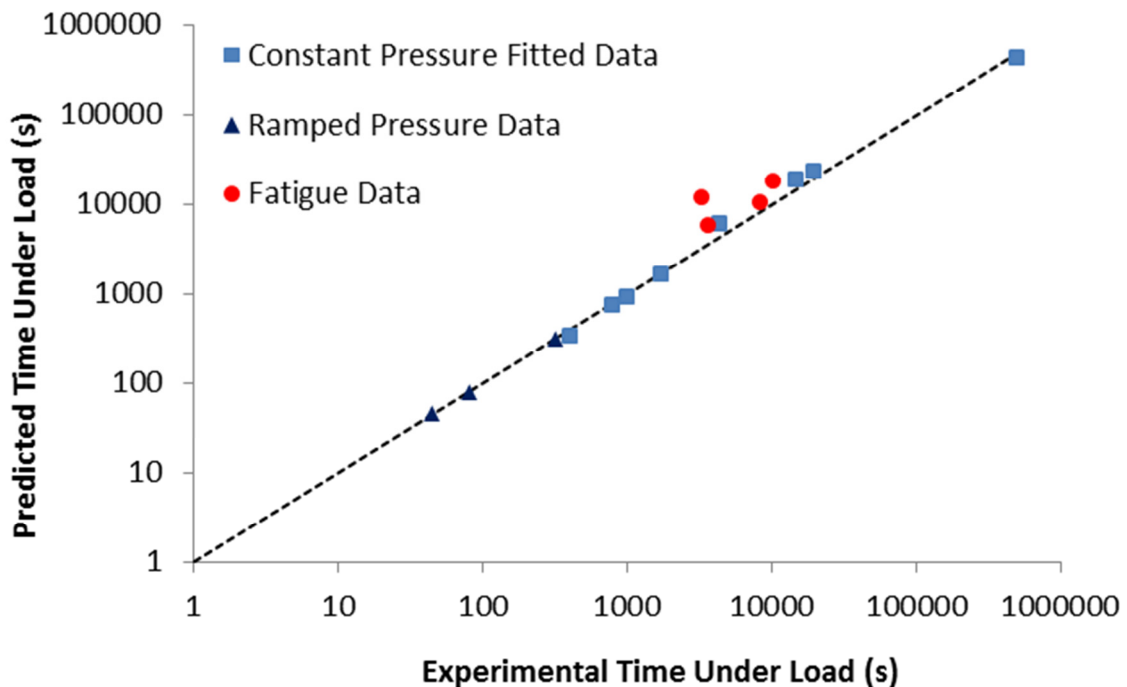
Figure 3-12: Summary of blister predictions plotted against time under load. Perfect agreement would fall directly on the line. From the plot, the predictions compare favorably, although fatigue loading is consistently predicted longer. This is likely due to loading effects that are not taken account due to the simplicity of the LDA model.

In Figure 3-12, perfect model agreement would fall directly on the dotted line that marks a slope of 1. The ramped pressure predictions agree very well with the experimental

measurements and fall directly along this line. The fatigue data shows good agreement as well, though the model consistently predicts longer lifetimes than what is experimentally seen. This can be attributed to the models inability to take into account damage that may occur due to the fatigue process, as it only accounts for the time under load, illustrating the need for a fatigue term. Despite that, three of the fatigue data points fall within the same scatter as the constant pressure data that developed the model and the second 10-4 duty cycle test shows only a factor of 3.5 difference between predicted and experimental time under load (Table 3-3). It is encouraging to note that the accuracy of prediction does not seem to be affected by the changing duty cycle, indicating robustness of the model in dealing with multiple types of loadings.

Conclusions

This study presents a lifetime prediction method using linear damage accumulation that analyzes PEM in a biaxial stress state without using constitutive data, significantly reducing complications in the strength analysis of pressure-loaded blister tests of PEMs. The method employs the use of digital image correlation and blister testing to measure the deformation and mimic the failure mode in a fuel cell, respectively. In this application, the study made five key simplifying assumptions:

1.) Quasi-static equilibrium condition is satisfied
2.) The blister geometry can be approximated as a sphere in the central portion where failure occurs
3.) The material undergoes constant volume deformation
4.) The stress-life curve fits a power law form
5.) The stress is treated as an average through the membrane thickness, although the material is a composite containing a reinforcing layer

Failure was predicted accurately for ramped pressure and over-predicted for fatigue pressure blister tests using this method, based on data taken under constant pressure testing to calculate the damage parameters. This transference of damage parameters from one loading profile to another implies accuracy in the stress approximations used and the possibility of extending this testing procedure to predict other biaxial stress loadings, i.e. hygrothermal. It also suggests the applicability of the LDA model, although it appears to require the addition of a fatigue term.

Acknowledgments

Chapter 4: Quantifying Mechanical Differences of a Partially Fluorinated Aromatic Hydrocarbon Ionomer blended with a PVDF Copolymer for use as a PEM

Abstract

The proton exchange membrane market has been dominated by Nafion® products. However, these products are relatively expensive to produce and thus introduce difficulties in reaching the DOE's target fuel cell costs. To circumvent this issue, research is becoming increasingly focused on membranes with hydrocarbon backbones; hydrocarbons materials are easily mass produced and therefore significantly less expensive than their Nafion® counterparts. Using digital image correlation and pressure loaded blister testing the mechanical strength of a hydrocarbon and Kynar Flex® blend developed for use as a proton exchange membrane in fuel cells are tested under two different pretreatments. A mechanical comparison of the pretreatments showed a significant strength improvement of the material subjected to a 100°C isothermal hold for 2 hours over the material that was not subjected to such a hold. This was shown to correspond to changes in both constitutive data and morphological properties that are consistent with both crystallinity appearing in the Kynar Flex® and limited chemical crosslinking.

Introduction

The fuel cell is a promising alternative to combustion engines for use in the transportation market. This is due to their ability to electrochemically convert hydrogen and oxygen efficiently into electrical energy with little or no harmful byproducts. An important feature of the fuel cell is the proton exchange membrane (PEM) that separates the anode and the cathode side of the reaction and allows current to be created. To run at peak efficiency there must be no gas crossover between the anode and a cathode side, which means the mechanical integrity of the PEM must be maintained through multiple temperature and humidity cycles. The Department of Energy has set the goal for fuel cells to be at $30/kW and 5000 hours of operation above 60% efficiency by the year 2015 [1]. This remains a difficult mark to reach especially with the industry standard PEM Nafion®, and its various derivatives, which are expensive, due to the polytetrafluoroethylene (PTFE) backbone, and provide low efficiency during high temperature and low humidity operation [44].

In recent years, efforts have been re-established in developing membranes that contain hydrocarbon backbones. In the past, hydrocarbon membranes had been investigated due to their ability to be inexpensively produced, but were abandoned due to low chemical and thermal stability [44]. In humidity cycling, Lai et al. found hydrocarbon membranes to be significantly less durable than Nafion® membranes [10]. Recently however, hydrocarbon membranes have become more viable due to their low cost and water uptake abilities making them reasonable for use in a wide range of environments. To improve the mechanical durability of hydrocarbons, General Motors has blended a partially fluorinated aromatic hydrocarbon (which will be

designated as PFCB for simplicity) ionomer with Kynar Flex®, a PVDF copolymer. The chemical structure of the PFCB ionomer and the Kynar Flex® copolymer is given in Figure 4-1.
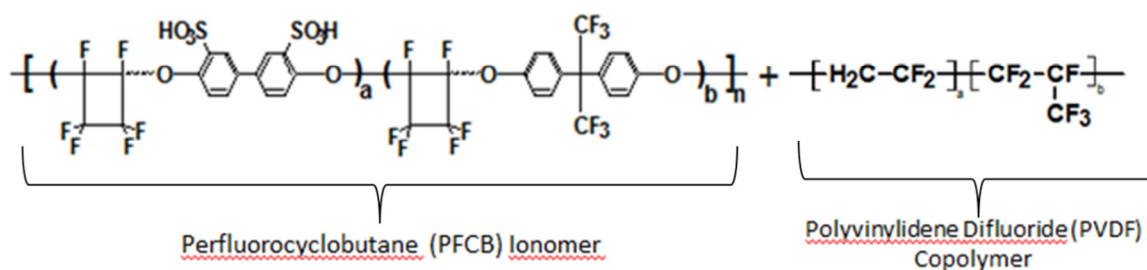
Figure 4-1: Chemical Structure of the Kynar Flex® copolymer (Right) and chemical structure of the PFCB ionomer (Left)

Initial durability studies showed that pure PFCB material shows brittle fracture behavior under dry conditions at strains much lower than maximum immersed elongations. The addition of Kynar Flex® in varying weight percent was found to improve the fracture behavior while not detrimentally affect the ion exchange capacity [45]. Morphologically, Kynar Flex® is known to show crystallinity under certain conditions, which would also tend to improve material strength. Partially fluorinated perfluorocyclobutane polymers with 6F linkages such as the PEMs investigated have also shown crystallinity [46].

The material properties of proton exchange membranes have been investigated extensively using numerous methods. Liu et al. examined the ultimate strength, elongation at break, and yield stress of Nafion® under uniaxial tension [21]. Silberstein et al. looked at the constitutive behavior of Nafion® using uniaxial testing [7] and biaxial cruciform testing [15]. Dillard et al. have used the blister test as a measurement of biaxial membrane strength to failure with a gas leakage criterion [24]. In this work, the previously mentioned PFCB membrane was mechanically tested after two different pretreatments. The differences in mechanical properties and morphological differences between the two treatments are discussed.

Experimental Techniques

Before testing, the membrane samples were placed into a water bath at 50°C for 1 hour to release any residual N,N-dimethylacetamide (DMAc) that remained from the casting process. Residual DMAc was seen to change ex-situ material properties because of the short time-scale of tests, but was not expected to affect in-situ behavior due to the material reaching "steady-state" quickly; that is, the DMAc is expected to be released after only a relative few automotive duty cycles. The water bath procedure was found to remove most of the DMAc in the material and better approximate the "steady-state" material behavior [47]. Bathing was completed in a frame to facilitate the drying process and keep the membrane free of wrinkles. The frame was made from two pieces of Teflon® that could be clamped together with screws, sandwiching the material between the pieces. It was then allowed to dry in a desiccator in the frame for approximately 24 hours before being removed for testing. Membranes undergoing only that

pretreatment before testing were designated as WBUN (Water Bath, Unannealed). A further pretreatment step included a 2 hour isothermal hold at 100°C. Such membranes were designated as WBAN (Water Bath, Annealed). The PFCB membranes tested were cast at different casting facilities, although they are chemically identical, and they will be fully designated by where they were cast. The designation BR10 is the PFCB ionomer blended with 30% Kynar Flex® at 18-22 microns of thickness depending on the pretreatment, and it was used for a majority of the testing procedures. BM7646 is PFCB ionomer blended with 30% Kynar Flex® with a thickness of 12 microns was used for DMA testing.

Blister Testing

Constant pressure and ramped pressure blister tests were performed at 90°C and 8% relative humidity on WBAN and WBUN BR10 membrane to examine the differences in biaxial strength and yield stress of the materials. Constant pressure testing was completed using the eight station blister fixture presented in [25,27]. The pressures were normalized for initial thickness differences as shown in Eqn. 4.1, which uses the Hencky linear elastic analysis as a guide [28].

$$P_{Norm} = \left[\frac{P}{t_0}\right]^{2/3} \qquad\qquad 4.1$$

Ramped pressure testing was completed with the use of the GOM ARAMIS 3D digital image correlation (DIC) system to examine the biaxial stress-strain curve of the materials. True stress was calculated by applying thin-walled spherical pressure vessel theory in the central region of the material and assuming constant volume deformation to calculate the thickness change from the surface strains. True stress and strain are given by Eqns. 4.2 & 4.3 respectively.

$$\sigma_{true}(t) = \frac{p(t) \cdot R(t)}{2h_0} \lambda_1(t)\lambda_2(t) \qquad\qquad 4.2$$

$$\varepsilon_{true}(t) = \ln(\varepsilon_1(t) + 1) = \ln \lambda_1(t) \qquad\qquad 4.3$$

Dynamic Mechanical Analysis

A thermal master curve referenced to 70°C and 30% RH was obtained for both WBUN and WBAN BM7646 membrane using TA Instruments Q800 dynamic mechanical analyzer in relaxation mode. The uniaxial stress relaxation measurements were performed at a strain level of 0.5% and temperature was incremented by 10°C from 30°C to 110°C. A hygrothermal master curve was also created for the WBAN BM7646 membrane by shifting the thermal master curves of multiple relative humidity levels.

Small Angle X-Ray Scattering

Small angle X-ray scattering (SAXS) is a common technique used to evaluate polymer domain sizes by shooting a sample of material with an x-ray beam and capturing the scattering angle of the X-rays. For small angle scattering, feature sizes on the order of nanometers are being measured, and as the scattering angle increases the feature sizes being measured decreases. For in depth information on theory behind SAXS, refer to [48]. In this work, SAXS data was collected by Nathan May and Mingqiang Zhang on WBAN BR10 and WBUN BR10 to analyze differences in ionic domain size as well as observe Kynar Flex® crystallinity. The measurements were taken at room temperature in a vacuum, corresponding to dry conditions.

Solvent Dissolution

A qualitative solvent dissolution study was performed on WBAN and WBUN BR10 membrane using DMAc as a solvent. The amount of DMAc added was 9x the weight of the membrane, creating a 10% by weight solution, similar to the weight percent of DMAc used during the initial casting of the membranes. The state of the membrane in solution was observed after 1 hour. The study was then repeated on a membrane cast from the pure ionomer (0% Kynar Flex®) to separate the effects of blending in Kynar Flex®.

Results

The annealing pretreatment was found to have a significant impact on the geometry of the sample. To quantify this change, two strips of WBUN BR10 were cut and two dots were placed along the length of each sample. These were then measured using calipers accurate to 0.02 mm. The thickness was measured using a drop micrometer accurate to 0.5 microns. Eight thickness measurements were taken over the sample and averaged to give the final value. The material was measured while sitting at ambient conditions (25°C and 45% RH) pre-anneal, directly after annealing (<5 min), and after approximately one week at ambient conditions. Table 1 summarizes the findings.

Table 4-1: Summary of geometric changes due to annealing procedure at 100°C for 2 hours

	L_0	h_0	L <5 min	h <5 min	L ~7 days	h ~7 days
Trial 1	74.20 mm	22.60 μm	76.00 mm	20.80 μm	76.30 mm	20.90 μm
Trial 2	59.00 mm	23.10 μm	61.30 mm	20.60 μm	61.30 mm	21.10 μm

The data corresponds to approximately 7-8% thickness reduction and 4% length increase, which corresponds to a volume contraction of approximately 2%. This apparent densification would be extremely significant as it is quite a large change for a polymer, but to be certain as to the magnitude more precise testing must be completed. Densification is possibly a result of crystallinity or chemical crosslinking of the blend. Further work showed that a one hour water bath at 50°C or 100°C did not return the membrane to its initial state.

Blister Testing

      Constant pressure blister testing performed on both systems showed a significant increase in material strength for the WBAN BR10 as compared to the WBUN BR10. Figure 4-2 shows the differences based on the Hencky normalization from Eqn. 4.1.
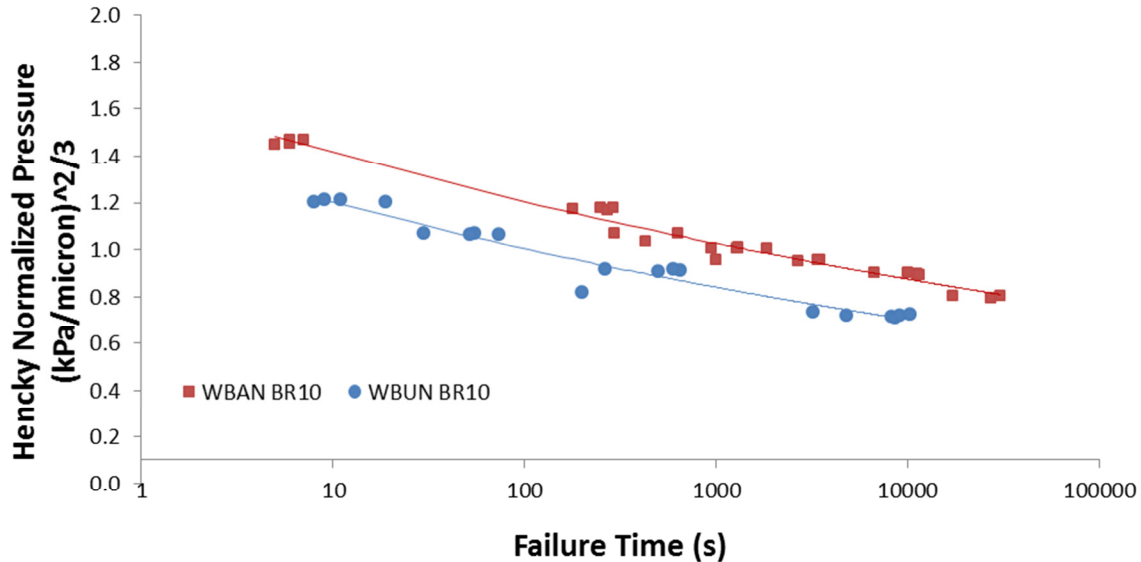
Figure 4-2: Strength difference of WBAN and WBUN BR10 at 90°C and 8% RH, showing improvement of strength in blister tests of the WBAN membrane over the WBUN membrane

      The figure shows significant lifetime differences between the WBAN and WBUN BR10 membrane. This difference was again found in the biaxial stress-strain plot and is shown in Figure 4-3. The initial biaxial modulus was found to be 739 MPa for the WBAN BR10 while it was only 397 MPa for the WBUN material. Perhaps more importantly for the blister test, which consists of significant deformation after yielding, the yield strength of the WBAN BR10 was 7.6 MPa compared to 5.3 MPa for the WBUN BR10. Yield was determined by the intersection of two lines describing the initial response and the yield response, as is shown in [7]. After yielding, the two materials appear to behave similarly, although the WBAN BR10 is offset due to the higher initial yield stress. This increased modulus and increased yield stress is in agreement with the pressure life data shown previously.
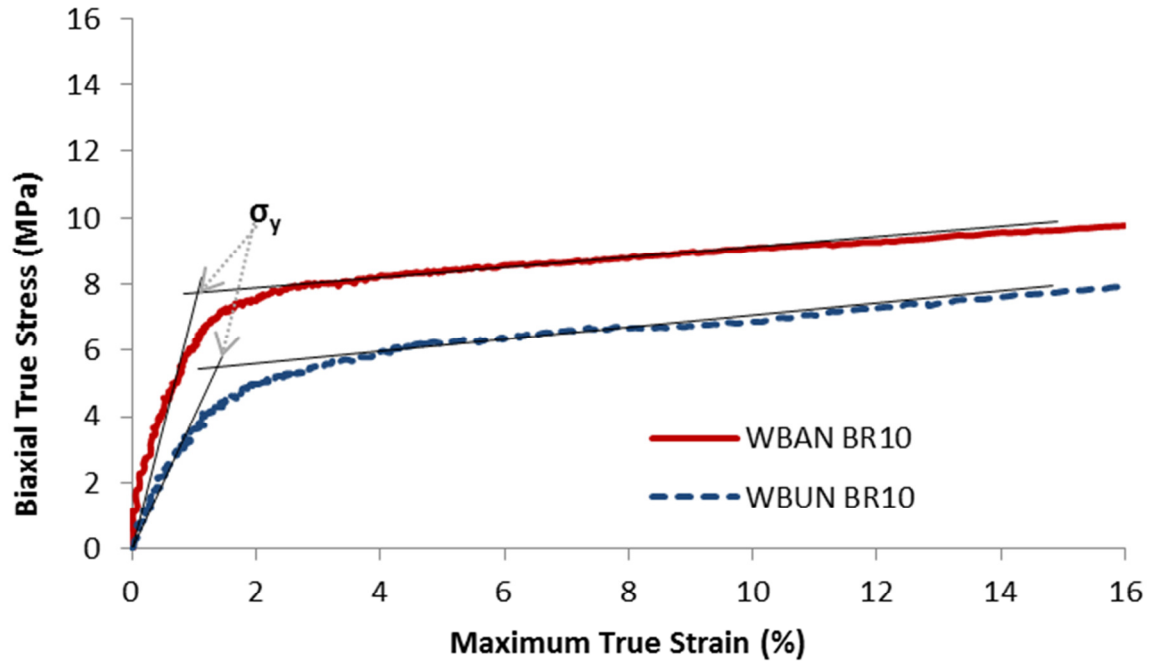
Figure 4-3: Ramped pressure blister stress-strain comparison of WBAN and WBUN BR10 membrane at a ramp rate of 0.056 kPa/s

DMA Analysis

Figure 4-4 shows the DMA results for the WBAN and WBUN BM7646 materials.
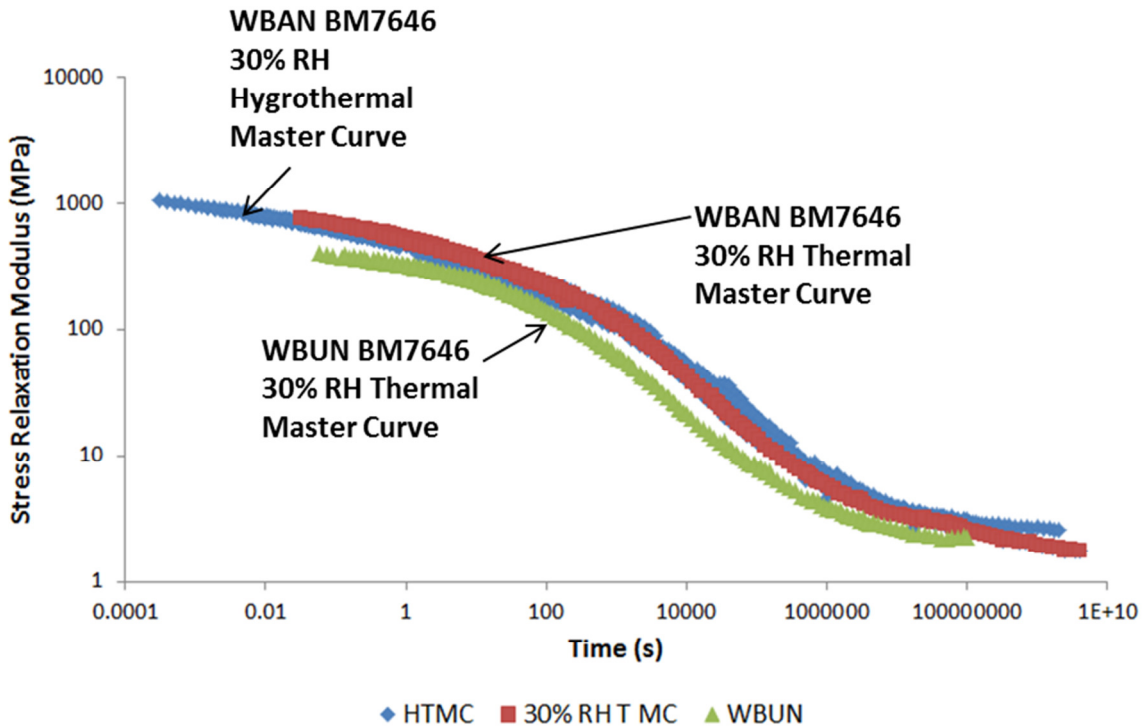
Figure 4-4: Relaxation modulus of BM7646 measured from small strain relaxation tests using DMA. Data collection and reduction by Katherine Finlay,

These results show that the hygrothermal master curve and the thermal master curve both agree well for the WBAN BM7646 and encourage belief in the measured behavior. The WBUN BM7646 was seen to be approximately half the modulus of the WBAN material at all locations on the curve, which more appropriately corresponds to a faster relaxation time. This observation corroborates the differences seen in blister testing. The WBUN BR10 deforms and fails more quickly due to its faster relaxation time.

Small Angle X-Ray Scattering

Small angle X-ray scattering data shows a slight difference between the WBAN BR10 and WBUN BR10. The most important difference is circled in Figure 4-5. This morphology has been shown by Nathan May to relate to Kynar Flex® crystallinity [N. May, personal communication, June 2011]. This slight increase in crystallinity was the first morphological difference observed between the materials.
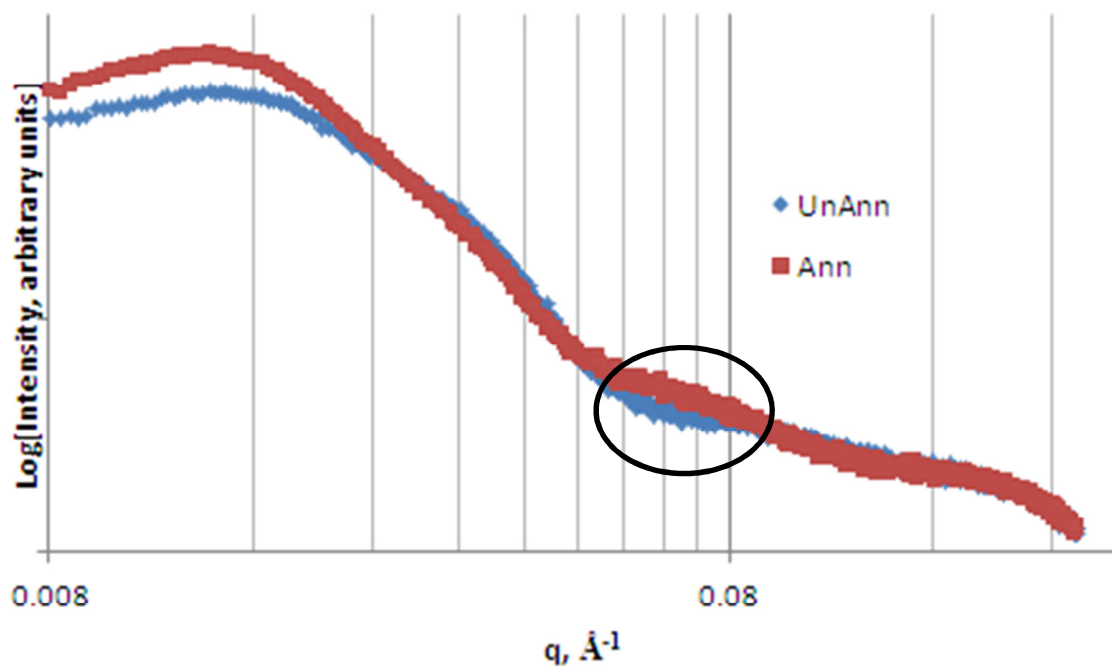
Figure 4-5: Comparison of SAXS data for WBAN BR10 (Ann) and WBUN BR10 (UnAnn) showing higher Kynar Flex® crystallinity in the WBAN sample. Thanks to Mingqiang Zhang for taking the SAXS data

Solvent Dissolution

The addition of a 10% DMAc solution to both the WBAN BR10 and WBUN BR10 provided qualitatively different results for each material. As can be seen in Figure 4-6 the WBAN BR10 does not dissolve after an hour under these conditions, while the WBUN BR10 dissolves completely after this time period. The WBAN BR10 remained solid at the time of writing this paper after many weeks sitting in the 10% solution. This was first thought to be a

consequence of the crystallinity in the Kynar Flex® seen in the SAXS data. However, further efforts have shown that pure PFCB ionomer (0% Kynar Flex®) after annealing behaves the same as the WBAN BR10 in 10% DMAc solution.
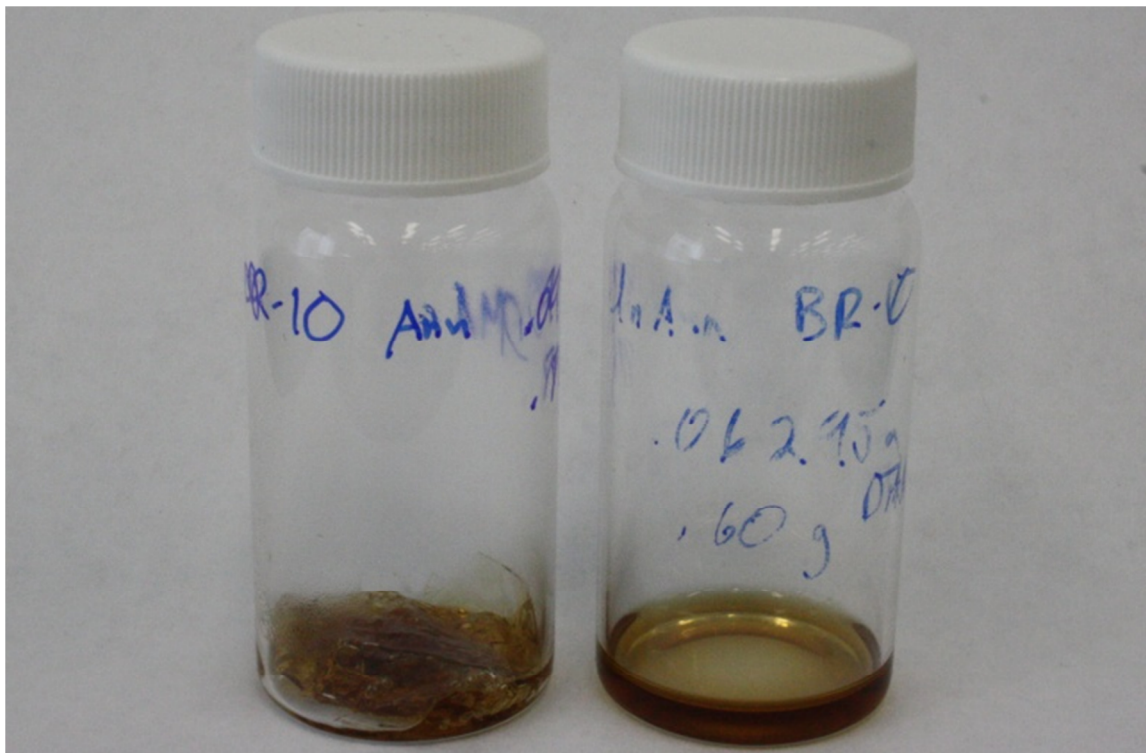
Figure 4-6: BR10 WBAN (Left) and WBUN (Right) in 10% by weight solution of DMAc after 1 hour. Obvious differences caused by the 100°C isotherm cause the WBAN membrane not to dissolve while the WBUN membrane does[N. May, personal communication, June 2011]

Conclusions

The previous data suggests that significant morphological changes occurred during the 100°C isothermal hold. This is evident from both the improved mechanical behavior and the differences in morphological tests completed. A possible conclusion is that the water channels in the material were collapsed during the annealing process due to water leaving. This would lead to the densification of the material and the apparent stiffness changes could be caused by decreased hydration. However, boiling the membrane was expected to rehydrate these channels and return the membrane to its original state, which was not observed.

The presence of Kynar Flex® crystallinity undoubtedly improves the mechanical strength of the material, but the results of the solvent dissolution study made it clear that this was not the only morphological effect, as WBAN BR10 and WBAN unblended PFCB ionomer were both found to be resistant to dissolution. If this resistance were based in the Kynar Flex® crystallinity, that would not be the case. Therefore, the ionomer must be undergoing morphological changes as well. Whether those changes are formation of crystallinity or chemical crosslinks between the sulfonate groups is presently uncertain. Crystallinity in perfluorocyclobutyl materials has been

seen in literature in the presence of 6F [46]. If crosslinking were occurring between the sulfonate groups, it would have to be a small amount to allow the material to show the definite yield behavior that is seen.

Work in this area is needed to fully develop an understanding of the morphological changes this material is undergoing. Measuring changes in ion exchange capacity would give insight into the number of sulfonate groups devoted to chemical crosslinks. Fourier transform infrared spectroscopy (FTIR) could also be used to further evaluate the extent of chemical crosslinking in the material.

Acknowledgements

Chapter 5: Conclusions and Future Work

This chapter has two purposes. The first is to briefly highlight the conclusions of the previous chapters so that they are succinctly stated. The second is to analyze the future direction of the work and guide the reader into thinking about further progress.

Conclusions

Chapter 2 was an introduction to the use of the DIC with the blister test. A method was developed to measure the blister test deformation over time without changing the membrane's behavior and use that information to evaluate its constitutive properties. Major conclusions from this chapter were:

- Speckling membranes with commercial spray paint significantly decreased the lifetimes, but the use of India ink provided a speckling method that preserved the material properties
- Using a fixture capable of backlighting the blister improved the overall coverage of DIC measurements throughout the blister lifetime and allowed for transparent materials to be tested (such as Nafion® NR-211) along with other translucent materials (such as Gore-Select® series 57)
- A spherical fit to the central region of the blister, measured using DIC, provides an excellent approximation to the blister geometry and stresses can be calculated using thin-walled spherical pressure vessel theory
- Biaxial stress-strain curves can be produced under ramped pressure loading that agree well with modulus data from literature. The strain rate is difficult to control, but can be tweaked using different pressure ramp rates

Chapter 3 used the stress profiles over the lifetime of the blister test as a basis for a linear damage accumulation model of the Gore-Select® series 57 membrane at 90°C and nominally dry conditions. Major conclusions from this chapter showed:

- A linear damage accumulation model could be reasonably fit to constant pressure data using a power law form of the stress life curve and solve for the damage parameters A and B
- Failure of both ramped pressure and fatigue pressure tests were reasonably predicted using the stresses calculated from the DIC data and the damage parameters developed with the constant pressure to failure model

Chapter 4 used the blister test and examined the constant pressure-lifetime differences between WBAN BR10 membrane and WBUN BR10 membrane. DIC was used with ramped pressure blister testing to measure the difference in biaxial modulus and yield strength and DMA testing

was completed to observe constitutive differences uniaxially. Morphologically, SAXS and solvent dissolution studies were compared.

- The 100°C annealing procedure produced significant geometric changes that resulted in slight densification of the material. This densification may be attributed to the increased Kynar Flex® crystallinity or chemical cross-linking but further work is needed to be sure
- Constant pressure blister test results showed that WBAN BR10 lasted longer than WBUN BR10 under the same pressure loadings, implying a higher material strength
- Ramped pressure blister tests showed that the initial biaxial modulus of the WBAN BR10 was higher than the WBUN BR10 material and it yielded at a correspondingly higher stress. This agrees well with the conclusion from the constant pressure testing data that shows the WBAN BR10 blister test have longer failure times
- DMA data showed that WBUN BM7645 relaxed approximately a half decade faster than WBAN BM7645, corresponding to an apparent factor of 2 stiffness difference. This difference corresponds well to the factor of 1.85 difference biaxially found for WBAN/WBUN BR10 membrane
- SAXS data showed an increase in Kynar Flex® crystallinity in the WBAN membrane that is hypothesized to contribute to the improvement in mechanical behavior, but the extent to which this contributes must be further investigated
- WBAN BR10 does not dissolve in a 10% by weight DMAc solution while WBUN BR10 does within minutes. This may be a side effect of the increased Kynar Flex® crystallinity, but the same behavior was found to occur in the pure PFCB ionomer. That implies the existence of chemical cross-links or significant increase of crystallinity in the PFCB ionomer, although these have not been seen directly

Future Work

There remains a significant amount of work left to properly connect a fuel cell operation cycle and the strength evaluation techniques that have been developed in this thesis. Although it was shown that the DIC is a good method for measurement of the blister behavior, and that blister failure in one loading profile can be used to predict failure of other loading profiles, creating an accurate strength model to predict in-situ fuel cell failure still remains to be seen. Some suggestions of where to look are presented below, as well as other possibilities that are either necessary or interesting or both.

- Perhaps a more relevant failure model for the blister test is the use of a fracture model as opposed to a stress accumulation model. It was observed that there were three main failure modes of the blister. These are bursting at large strains, leaking at large strains, and leaking at low strain. A stress accumulation model is purely phenomenological and, although it predicts failure times well for materials that show consistent behavior, it does not predict the different failure modes that are seen

- Finite element modeling with ABAQUS and DIC measurements should correlate well given that they both measure stresses based on deformations. This correlation should allow a variation of parameters technique to back calculate material behavior using DIC data and an FE model
- DIC could be used to understand the affect that initial membrane buckling has on the failure times of the blister test. Undoubtedly, buckling changes the behavior of the material over the lifetime, as well as under initial loading, but the extent to which this change affects the measured properties, specifically the material lifetime, is unknown. Ideally the membrane should be tested without any buckling, but that is impractical under the conditions of interest in fuel cells, which requires heating and dampening of the environment which generally swells the material
- The DIC data collected can be used to a much larger extent. Most of the work in this thesis focused on the central region near failure, but since DIC is full field the data can be processed full field. For example, DIC can be used to measure the local geometry of the blister and by assuming quasi-static equilibrium the local stresses over the entire surface may be calculated. Local stress versus local strain curves, although perhaps academic, would be an interesting result that would give insight into an analytical model
- Appendix E presents evidence that the flow rate significantly affects the failure time of Gore-Select® series 57 membranes and therefore most likely impacts the failure time of all membrane types. This might be expected if the loading times were orders of magnitude different, but that was not found, so the reason for this flow rate dependence is not known. Despite being somewhat academic, understanding this change in response is important for comparison between different blister fixtures
- The cause of the strength improvement and material stiffening between the WBAN and WBUN PFCB membranes needs further clarification. There are multiple possibilities, or most likely a combination of possibilities, that causes the material differences. FTIR and ion exchange capacity measurements could be used to check for chemical crosslinks of the sulfonate groups

References

1. US DEPARTMENT OF ENERGY. **Basic Research Needs for the Hydrogen Economy**. Office of Basic Energy Sciences. Washington DC. 2004.

2. O'HAYRE, R. et al. **Fuel Cell Fundamentals**. New York: John Wiley & Sons, 2006.

3. WANG, Y. et al. A review of polymer electrolyte membrane fuel cells: Technology, applications. **Journal of Applied Energy**, p. 981-1007, 2011.

4. MAURITZ, K. A.; MOORE, R. B. The State of Understanding of Nafion. **Chemical Reviews**, v. 104, p. 4535-4585, October 2004.

5. TANG, Y. et al. An experimental investigation of humidity and temperature effects. **Materials Science and Engineering**, v. 425, p. 297-304, 2006.

6. LAI, Y.-H. et al. Viscoelastic Stress Analysis of Constrained Proton Exchange Membranes Under Humidity Cycling. **Journal of Fuel Cell Science and Technology**, v. 6, 2007.

7. SILBERSTEIN, M. N.; BOYCE, M. C. Constitutive modeling of the rate, temperature, and hydration dependent. **Journal of Power Sources**, v. 195, p. 5692-5706, 2010.

8. ALBERTI, G.; NARDUCCI, R.; SGANAPPA, M. Effects of hydrothermal/thermal treatments on the water-uptake of Nafion. **Journal of Power Sources**, v. 178, p. 575-583, 2008.

9. SATTERFIELD, M. B.; BENZIGER, J. B. Non-Fickian Water Vapor Sorption Dynamics by Nafion Membranes. **Journal of Physical Chemistry**, v. 112, p. 3693-3704, 2008.

10. LAI, Y.-H.; DILLARD, D. A. Mechanical Durability Characterization and Modeling of Ionomeric Membranes. In: VIELSTICH, W.; YOKOKAWA, H.; GASTEIGER, H. A. **Handbook of Fuel Cells- Fundamentals, Technology, and Applications**. [S.l.]: John Wiley & Songs, v. 5, 2009. Cap. 27.

11. TANG, Y. et al. Stresses in Proton Exchange Membranes due to Hygro-Thermal Loading. **Journal of Fuel Cell Science and Technology**, v. 3, p. 119-124, May 2006.

12. HUMFELD JR, G. R.; DILLARD, D. A. Residual Stress Development in Adhesive Joints Subjected to Thermal Cycling. **Journal of Adhesion**, v. 65, 1998. ISSN 277-306.

13. LU, W. et al. The Effect of Pinholes on Proton Exchange Membrane Fuel Cell Performance. **International Journal of Energy Research**, p. 35; 24-30, 2010.

14. LIU, D.; CASE, S. W. Durability study of proton exchange membrane fuel cells under dynamic testing conditions with cyclic current profile. **Journal of Power Sources**, v. 162, n. 1, p. 521-531, November 2006.

15. SILBERSTEIN, M. N.; PILLAI, P. V.; BOYCE, M. C. Biaxial-elastic viscoplastic behavior of Nafion membranes. **The International Journal for the Science and Technology of Polymers**, v. 52, p. 529-539, 2011.

16. PATANKAR, K. A. et al. Nonlinear Viscoelastic Characterization and Modeling of Proton Exchange Membranes. **Journal of Polymer Science: Part B Polymer Physics**, August 2009.

17. LI, Y. **Ph.D. Dissertation: Experimental Studies on the Mechanical Durability of Proton Exchange Membranes**. Virginia Tech. Blacksburg, VA. 2008.

18. LI, Y. et al. **Measuring Hygrothermal Stresses in Proton Exchange Membranes**. SEM Annual Conference and Exposition on Experimental and Applied Mechanics. [S.l.]: Society for Experimental Mechanics. 2009. p. 332.

19. LI, Y. et al. Experimental Measurement of Stress and Strain in Nafion Membrane During Hydration Cycles. **Experimental Mechanics (In Review)**, 2011.

20. GITTLEMAN, C. S.; LAI, Y.-H. **Durability of Perfluoro Sulfonic Acid Membranes for PEM Fuel Cells**. Extended Abstract, the AIChE 2005 Annual Meeting. Cincinnati, OH: [s.n.]. 2005.

21. LIU, D. et al. Tensile Behavior of Nafion and Sulfonated Poly(arylene ether sulfone) Copolymer Membranes and Its Morphological Correlations. **Journal of Polymer Science Part B-Polymer Physics**, v. 44, p. 1453-1465, 2006.

22. PATANKAR, K. A. et al. Characterizing Fracture Energy of Proton Exchange Membranes Using a Knife Slit Test. **Journal of Polymer Science Part B- Polymer Chemistry**, v. 48, p. 333-343, 2010.

23. LI, Y. et al. Characterizing the Fracture Resistance of Proton Exchange Membranes. **Journal of Power Sources**, v. 185, n. 1, p. 374-380.

24. DILLARD, D. A. et al. On the Use of Pressure-Loaded Blister Tests to Characterize the Strength and Durability of Proton Exchange Membranes. **Journal of Fuel Cell Science and Technology**, 2007.

25. GROHS, J. R. et al. Evaluating the time and temperature dependent strength of Gore-Select series 57 proton exchange membrane using a pressure loaded blister test. **Journal of Power Sources**, v. 152, p. 527-531, 2010.

26. PESTRAK, M. T. **Master's Thesis: The Effect of Catalyst Layer Cracks on the Mechanical Fatigue of Membrane Electrode Assemblies**. Virginia Tech. Blacksburg, VA. 2010.

27. LI, Y. et al. Fatigue and Creep to Leak Tests of Proton Exchange Membranes Using Pressure-Loaded Blister Tests. **Journal of Power Sources**, v. 194, n. 2, p. 873-879, 2009.

28. HENCKY, H. Uber den spannungszustand in kreisrunden platten mit verschwindender biegungssteiflgkeit. **Zeitschrift fur Mathematik und Physik,** v. 63, p. 311-317, 1915.

29. BRINSON, H. F.; BRINSON, L. C. **Polymer Engineering Science and Viscoelasticy:** An Introduction. New York: Springer Science + Business Media, 2008.

30. GROHS, J. R. **Analysis and Modeling of the Mechanical Durability of Proton Exchange Membranes Using Pressure-Loaded Blister Tests**. Virginia Tech. Blacksburg, VA. 2009.

31. PESTRAK, M. et al. The effect of Mechanical Fatigue on the Lifetimes of Membrane Electrode Assemblies. **Journal of Fuel Cell Science and Technology**, 2010.

32. VLASSAK, J. J.; NIX, W. D. A new bulge test technique for the determination of Young's modulus and Poisson's ratio of thin films. **Journal of Materials Research**, v. 7, n. 12, p. 3242-3249, December 1992.

33. G, A. M. et al. Micro-Fabricated Structures for the In-Situ Measurement of Residual Stress, Young's Modulus, and Ultimate Strain of Thin Films. **Applied Physics Letters**, Woodbury, v. 51, n. 4, p. 241-243, 1987.

34. XU, D.; LIECHTI, K. M. Bulge Testing Transparent Films with Moire Deflectometry. **Experimental Mechanics**, v. 50, p. 217-225, 2010.

35. FEDOROV, A.; VELLINGA, W. P.; AND DE HOSSON, J. T. M. Effects of tensile and compressive in-plane stress fields on delamination in laser induced adhesion experiments. **Journal of Applied Physics**, v. 103, n. 10, p. 103523-7, 2008.

36. JIN, H.; LU, W. Y.; KORELLIS, J. Microscale deformation measurement using the digital image correlation technique and scanning electron microscope imaging. **The Journal of Strain Analysis for Engineering Design**, v. 43, p. 719-728, 2008.

37. GOM OPTICAL MEASURING TECHNIQUES. **ARAMIS User Manual-Software**. Braunschweigh, Germany, p. 122. 2007.

38. TSAKALAKOS, T. The Bulge Test: A comparison of theory and experiment for isotropic and anisotropic films. **Thin Solid Films**, v. 73, p. 293-305, 1981.

39. PATANKAR, K. A. et al. Hygrothermal characterization of the viscoelastic properties of Gore-Select® 57 proton exchange membrane. **Mechanics of Time Dependent Materials**, v. 12, p. 221-236, 2008.

40. BEER, F. P. et al. **Mechanics of Materials**. New York: McGraw-Hill, 2009.

41. WILLEMS, A. et al. Optical Strain Fields in Shear and Tensile Testing of Textile Reinforcements. **Composites Science and Technology**, v. 68, n. 3-4, p. 807-819, 2008.

42. DOWLING, N. E. **Mechanical Behavior of Materials**. 3rd. ed. Upper Saddle River: Pearson Prentice Hall, 2007.

43. CHRZANOWSKI, M. Use of the Damage Concept in Describing Creep-Fatigue Interaction Under Prescribed Stress. **International Journal of Mechanical Science**, v. 18, p. 69-73, 1976.

44. RIKUKAWA, M.; SANUI, K. Proton-Conduction Polymer Electrolyte Membranes based on Hydrocarbon Polymers. **Progress in Polymer Science**, v. 25, n. 2000, p. 1463-1502, May 2000.

45. MACKINNON, S. M.; FULLER, T. J.; GITTLEMAN, C. S. **Perfluorocyclobutane Based PEM for Automotive Fuel Cells**. General Motors Corporation. Honeoye Falls. 2009.

46. SMITH JR, D. W. et al. Anomalous crystallinity in a semi-fluorinated perfluorocyclobutyl (PFCB) polymer contain the hexafluoro-i-propylidene (6F) linkage. **Polymer Communication**, Clemson, v. 45, p. 5755-5760, June 2004.

47. LI, Y. **Hygral thermal treatment of BM 7645 membrane**. General Motors Electrochemical Energy Research Lab. Honeoye Falls. 2010.

48. GLATTER, O.; KRATKY, O. (Eds.). **Small Angle X-Ray Scattering**. London: Academic Press, Inc. , 1982.

Appendix A: Raw DIC Stress Profiles of Gore-Select® series 57 Membrane at 90°C Nominally Dry Conditions

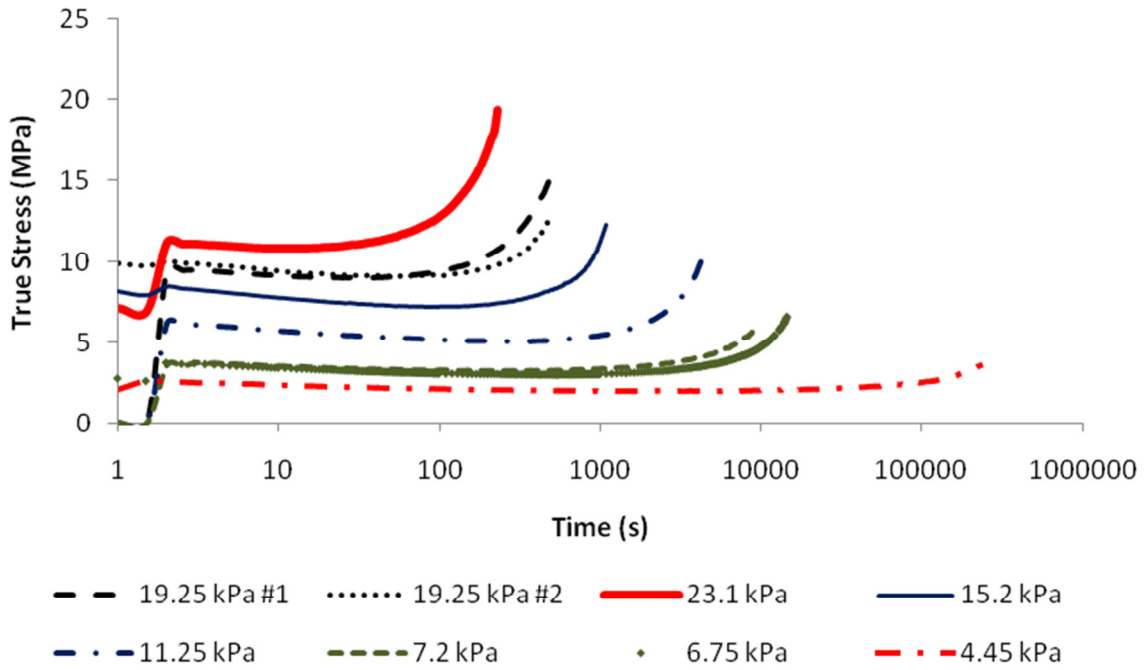**Figure A 1: DIC true stress data of constant pressure tests used to calculate the damage parameters A and B**
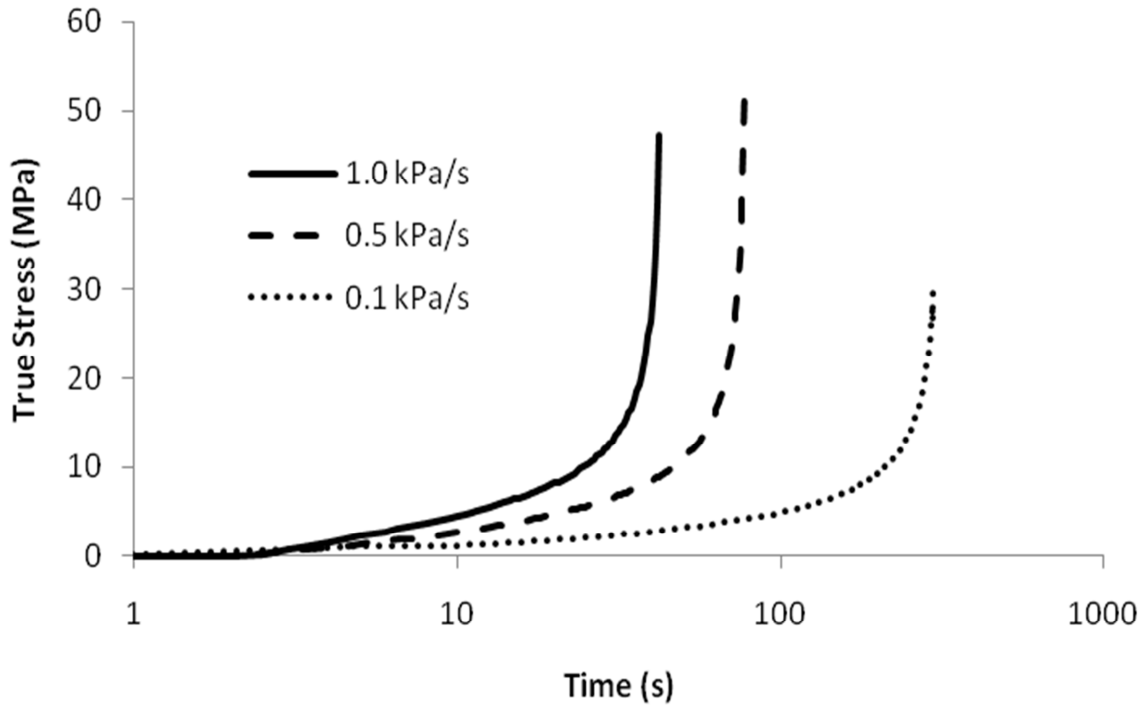
Figure A 2: DIC true stress profiles of ramped pressure tests used for predicting failure based on the constant pressure damage parameters developed
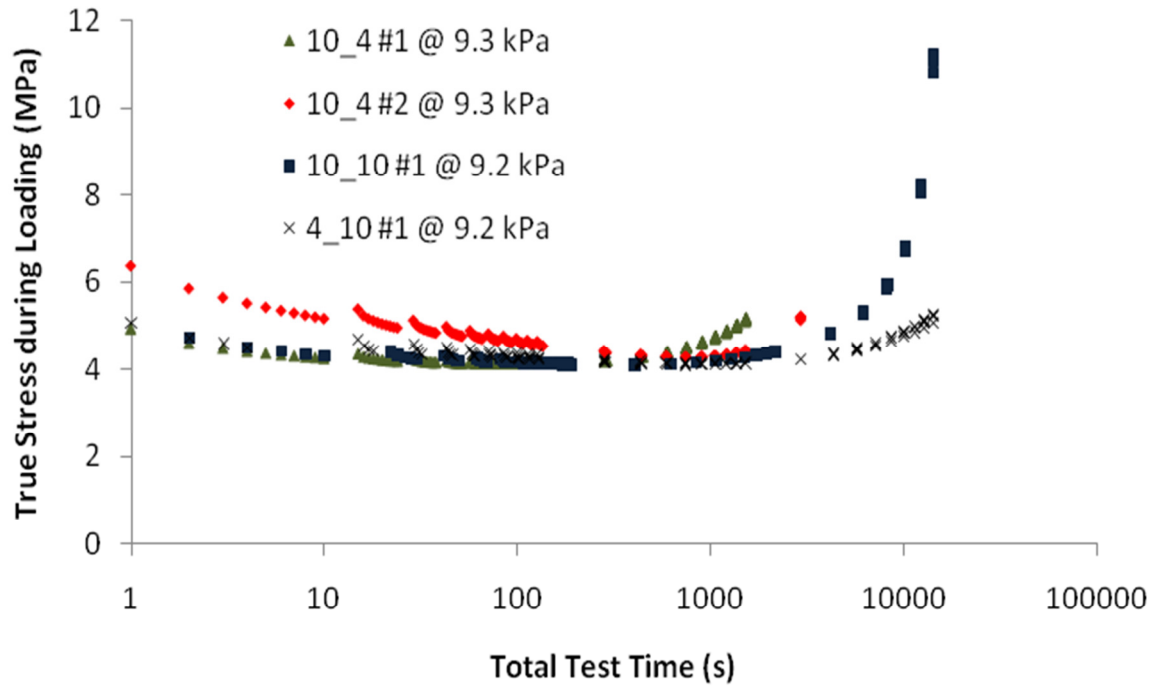
Figure A 3: DIC true stress profiles of fatigue pressure testing under multiple duty cycles, plotting only the loading portion

Appendix B: MATLAB program used to import and center data from DIC text files by assuming axi-symmetry

```matlab
%% Importing Data

% This file will import multiple text data files from the DIC
% Data files must be in the same directory, which must be open
% Import File organized as
%       Time Index_X Index_Y {Xcoord Ycoord Zcoord}_Undeformed {Xcoord Ycoord
Zcoord}_Deformed StrainMaj StrainMin
% Strain Values may not be calculated at points that lie on the boundary
% resulting in NAN. All other values will exist

files=dir('*.txt');             %Importing text files into vector
num=length(files);              %Allocating number of files for looping
%%%%
%number of data columns
    a=11;
%number of strain columns
    b=2;

Inputs=cell(num,1);Unorganized=cell(num,1);
org=zeros(num,2);Undeformed=cell(num,1);
i=1;q=1;
while i<=num
    Temp_Data=[];
    data=importdata(files(q).name);
    m=length(data);
    if m>=300        %Sets a minimum number of data points the set must have
        n=1;
        for j=1:m
            if isnan(data(j,3))     %Fixes strain overflow if occurs,
discounts border points
            Temp_Data(n,:)=[i data(j-1,2:end) data(j,1:b)];
            n=n+1;
            end
        end
    org(i,:)=[data(1,1) i];
    Unorganized{i}=Temp_Data;
    else
        i=i-1;
        num=num-1;
    end
    i=i+1;q=q+1;
end
B=sortrows(org);
y=length(org)-num;
B=B(y+1:num+y,:);
for i=1:num
    for j=1:num
    if B(i,2)==Unorganized{j}(1,1)
        Inputs{i}=[Unorganized{j}(:,2:3) Unorganized{j}(:,7:a)];
        Undeformed{i}=Unorganized{j}(:,4:6);
        break
```

```matlab
        end
    end
end
time=B(:,1);
Inputs=Inputs(1:length(Inputs)-y);
Undeformed=Undeformed(1:length(Inputs)-y);
Number_of_Stages=length(Inputs);
% clearing unneccessary variables
plot(sqrt(Inputs{4}(:,3).^2+Inputs{4}(:,4).^2),Inputs{4}(:,5),'.')


clear B Temp_Data Unorganized ans data files i j m n org q y num
%% Centering the data on x and y
Optimization_Stage=round(Number_of_Stages/5);
% Optimization_Stage=5;
% Assume that the data is centered and use that as a basis to start
x0=0;y0=0;
    [~,gof]=fit(sqrt((Inputs{Optimization_Stage}(:,3)-
x0).^2+(Inputs{Optimization_Stage}(:,4)-
y0).^2),Inputs{Optimization_Stage}(:,5),'poly3');
    Sum_of_Squares=gof.sse;
for i=-10:.1:10
    for j=-10:.1:10
    [~,gof]=fit(sqrt((Inputs{Optimization_Stage}(:,3)-
i).^2+(Inputs{Optimization_Stage}(:,4)-
j).^2),Inputs{Optimization_Stage}(:,5),'poly3');
    if gof.sse<Sum_of_Squares
        Sum_of_Squares=gof.sse;
        x0=i; y0=j;
    end
    end
end
for i=x0-.1:.01:x0+.1
    for j=y0-.1:.01:y0+.1
    [~,gof]=fit(sqrt((Inputs{Optimization_Stage}(:,3)-
i).^2+(Inputs{Optimization_Stage}(:,4)-
j).^2),Inputs{Optimization_Stage}(:,5),'poly3');
    if gof.sse<Sum_of_Squares
        Sum_of_Squares=gof.sse;
        x0=i; y0=j;
    end
    end
end
for i=1:Number_of_Stages
    Inputs{i}(:,3)=Inputs{i}(:,3)-x0;
    Inputs{i}(:,4)=Inputs{i}(:,4)-y0;
%     Undeformed{i}(:,1)=Undeformed{i}(:,1)-x0;
%     Undeformed{i}(:,2)=Undeformed{i}(:,2)-y0;
end


%plotting to look at how collapsible the data is
plot(sqrt(Inputs{4}(:,3).^2+Inputs{4}(:,4).^2),Inputs{4}(:,5),'.')
hold on
plot(sqrt(Inputs{Optimization_Stage}(:,3).^2+Inputs{Optimization_Stage}(:,4).
^2),...
    Inputs{Optimization_Stage}(:,5),'r.')
```

```
plot(sqrt(Inputs{2*Optimization_Stage}(:,3).^2+Inputs{2*Optimization_Stage}(:
,4).^2),...
    Inputs{2*Optimization_Stage}(:,5),'g.')
% clearing unneccessary variables

fitt=fit(sqrt(Inputs{3}(:,3).^2+Inputs{3}(:,4).^2),Inputs{3}(:,5),'poly4');
plot(fitt,'k')

wmax=fitt.p5;
wmin=fitt.p1*9.525^4+fitt.p2*9.525^3+fitt.p3*9.525^2+fitt.p4*9.525+fitt.p5;
w0=wmax-wmin;
hold off




clear Sum_of_Squares ans gof i j fitt
```

Appendix C: Recursive MATLAB program used to fit LDA model to constant pressure data and output A and B damage parameters

This method simply uses brute force to minimize the error between the experimental and predicted lifetimes by stepping through multiple values of A and B.

```matlab
%% Linear Damage Accumulation Model
% Inputs
    %Stress_ConsVol{j}
    %Time{j}
    %Fit_Parameter
    %Exp_Failure
    %Strain{j}


PredFailure=zeros(length(Stress_ConsVol),1);
error=1e50;
Step=[1 10 100 1e3 1e4 1e5 1e6 1e7 1e8 1e9 1e10 1e11 1e12 1e13 1e14 1e15...
    1e16 1e17 1e18 1e19 1e20 1e21 1e22 1e23 1e24 1e25 1e26 1e27 1e28 1e29
1e30];

for i=1:length(Step)
    A=Step(i);
    for B=0:-1:-25
            for j=1:length(Stress_ConsVol)
                l=length(Stress_ConsVol{j});
                Integral=0;
                Integrand=(1/A)*Stress_ConsVol{j}.^(-B);
                for k=1:l-1
                Integral=Integral+0.5*(Time{j}(k+1)-
Time{j}(k))*(Integrand(k+1)+Integrand(k));
                    if k==l-1 && Integral<1
                        deltad=1-Integral;
                        part1=-B*Fit_Parameter(2,j)*Time{j}(k+1);
                        part2=-
B*Fit_Parameter(2,j)*A*Fit_Parameter(1,j)*deltad;
                        PredFailure(j)=-
log(exp(part1)+part2)/(B*Fit_Parameter(2,j));
                    elseif Integral>=1
                        PredFailure(j)=Time{j}(k+1);
                        break
                    end
                end
            end
            diff=sum((log10(Exp_Failure)-log10(PredFailure)).^2);
            if diff<error
                error=diff;
                Amin=A;
                Bmin=B;
            end
    end
end

 Astart=Amin;
 Bstart=Bmin;
```

```matlab
    for A=0.5*Astart:Astart/10:1.5*Astart
        for B=Bstart+0.5:-.1:Bstart-0.5
            for j=1:length(Stress_ConsVol)
                l=length(Stress_ConsVol{j});
                Integral=0;
                Integrand=(1/A)*Stress_ConsVol{j}.^(-B);
                for k=1:l-1
                Integral=Integral+0.5*(Time{j}(k+1)-
Time{j}(k))*(Integrand(k+1)+Integrand(k));
                    if k==l-1 && Integral<1
                        deltad=1-Integral;
                        part1=-B*Fit_Parameter(2,j)*Time{j}(k+1);
                        part2=-
B*Fit_Parameter(2,j)*A*Fit_Parameter(1,j)*deltad;
                        PredFailure(j)=-
log(exp(part1)+part2)/(B*Fit_Parameter(2,j));
                    elseif Integral>=1
                        PredFailure(j)=Time{j}(k+1);
                        break
                    end
                end
            end
            diff=sum((log10(Exp_Failure)-log10(PredFailure)).^2);
            if diff<error
                error=diff;
                Amin=A;
                Bmin=B;
            end


        end
    end

 Astart1=Amin;
 Bstart=Bmin;
    for A=Astart1-5*Astart/100:Astart/100:Astart1+5*Astart/100
        for B=Bstart+0.05:-0.01:Bstart-0.05
            for j=1:length(Stress_ConsVol)
                l=length(Stress_ConsVol{j});
                Integral=0;
                Integrand=(1/A)*Stress_ConsVol{j}.^(-B);
                for k=1:l-1
                Integral=Integral+0.5*(Time{j}(k+1)-
Time{j}(k))*(Integrand(k+1)+Integrand(k));
                    if k==l-1 && Integral<1
                        deltad=1-Integral;
                        part1=-B*Fit_Parameter(2,j)*Time{j}(k+1);
                        part2=-
B*Fit_Parameter(2,j)*A*Fit_Parameter(1,j)*deltad;
                        PredFailure(j)=-
log(exp(part1)+part2)/(B*Fit_Parameter(2,j));
                    elseif Integral>=1
                        PredFailure(j)=Time{j}(k+1);
                        break
                    end
                end
            end
```

```matlab
            diff=sum((log10(Exp_Failure)-log10(PredFailure)).^2);
            if diff<error
                error=diff;
                Amin=A;
                Bmin=B;
            end


        end
    end

 Astart1=Amin;
 Bstart=Bmin;
    for A=Astart1-5*Astart/1000:Astart/1000:Astart1+5*Astart/1000
        for B=Bstart+0.005:-0.001:Bstart-0.005
            for j=1:length(Stress_ConsVol)
                l=length(Stress_ConsVol{j});
                Integral=0;
                Integrand=(1/A)*Stress_ConsVol{j}.^(-B);
                for k=1:l-1
                Integral=Integral+0.5*(Time{j}(k+1)-
Time{j}(k))*(Integrand(k+1)+Integrand(k));
                    if k==l-1 && Integral<1
                        deltad=1-Integral;
                        part1=-B*Fit_Parameter(2,j)*Time{j}(k+1);
                        part2=-
B*Fit_Parameter(2,j)*A*Fit_Parameter(1,j)*deltad;
                        PredFailure(j)=-
log(exp(part1)+part2)/(B*Fit_Parameter(2,j));
                    elseif Integral>=1
                         PredFailure(j)=Time{j}(k+1);
                         break
                    end
                end
            end
            diff=sum((log10(Exp_Failure)-log10(PredFailure)).^2);
            if diff<error
                error=diff;
                Amin=A;
                Bmin=B;
            end

        end
    end

 Astart1=Amin;
 B=Bmin;
    for A=Astart1-5*Astart/10000:Astart/10000:Astart1+5*Astart/10000
            for j=1:length(Stress_ConsVol)
                l=length(Stress_ConsVol{j});
                Integral=0;
                Integrand=(1/A)*Stress_ConsVol{j}.^(-B);
                for k=1:l-1
                Integral=Integral+0.5*(Time{j}(k+1)-
Time{j}(k))*(Integrand(k+1)+Integrand(k));
                    if k==l-1 && Integral<1
                        deltad=1-Integral;
```

```
                            part1=-B*Fit_Parameter(2,j)*Time{j}(k+1);
                            part2=-
B*Fit_Parameter(2,j)*A*Fit_Parameter(1,j)*deltad;
                            PredFailure(j)=-
log(exp(part1)+part2)/(B*Fit_Parameter(2,j));
                        elseif Integral>=1
                            PredFailure(j)=Time{j}(k+1);
                             break
                        end
                    end
                end
                diff=sum((log10(Exp_Failure)-log10(PredFailure)).^2);
                if diff<error
                    error=diff;
                    Amin=A;
                    Bmin=B;
                end
    end

 Astart1=Amin;
 B=Bmin;
    for A=Astart1-5*Astart/100000:Astart/100000:Astart1+5*Astart/100000
            for j=1:length(Stress_ConsVol)
                l=length(Stress_ConsVol{j});
                Integral=0;
                Integrand=(1/A)*Stress_ConsVol{j}.^(-B);
                for k=1:l-1
                Integral=Integral+0.5*(Time{j}(k+1)-
Time{j}(k))*(Integrand(k+1)+Integrand(k));
                    if k==l-1 && Integral<1
                        deltad=1-Integral;
                        part1=-B*Fit_Parameter(2,j)*Time{j}(k+1);
                        part2=-
B*Fit_Parameter(2,j)*A*Fit_Parameter(1,j)*deltad;
                        PredFailure(j)=-
log(exp(part1)+part2)/(B*Fit_Parameter(2,j));
                        elseif Integral>=1
                             PredFailure(j)=Time{j}(k+1);
                              break
                        end
                    end
                end
                diff=sum((log10(Exp_Failure)-log10(PredFailure)).^2);
                if diff<error
                    error=diff;
                    Amin=A;
                    Bmin=B;
                end
    end

 Astart1=Amin;
 B=Bmin;
    for A=Astart1-5*Astart/1000000:Astart/1000000:Astart1+5*Astart/1000000
            for j=1:length(Stress_ConsVol)
                l=length(Stress_ConsVol{j});
                Integral=0;
```

```
                Integrand=(1/A)*Stress_ConsVol{j}.^(-B);
                for k=1:l-1
                Integral=Integral+0.5*(Time{j}(k+1)-
Time{j}(k))*(Integrand(k+1)+Integrand(k));
                    if k==l-1 && Integral<1
                        deltad=1-Integral;
                        part1=-B*Fit_Parameter(2,j)*Time{j}(k+1);
                        part2=-
B*Fit_Parameter(2,j)*A*Fit_Parameter(1,j)*deltad;
                        PredFailure(j)=-
log(exp(part1)+part2)/(B*Fit_Parameter(2,j));
                    elseif Integral>=1
                         PredFailure(j)=Time{j}(k+1);
                         break
                    end
                end
            end
            diff=sum((log10(Exp_Failure)-log10(PredFailure)).^2);
            if diff<error
                error=diff;
                Amin=A;
                Bmin=B;
            end
        end
    end
    clear A Astart Astart1 B Bstart Integral Integrand integral Step diff
error i
    clear stress1 Integrand1 inside j k l part1 part2 q dt
```

Appendix D: Measuring Poisson's ratio at 90°C and nominally dry conditions using digital image correlation and relaxation testing

Using DIC to measure Poisson's ratio at operating temperatures of a fuel cell required the development of a new fixture that could fit inside the oven. The fixture was screw driven and attached to the top of the oven. A load cell was not added, since it is not needed for Poisson's ratio measurements, although it could be used to maintain consistency with other data. Figure D 1 shows the fixture.

Figure D 1: Image of Poisson's ratio fixture. It is a simple screw driven relaxation fixture that can be manually set to a given displacement. The load is not measured in this fixture since there is no load cell

The raw DIC data is shown in Figure D 2. Only the data in the central region of the specimen was taken, corresponding to approximately 25mm of gauge length. Over this region, the strain was averaged in the x and y directions and the average was used to calculate Poisson's ratio from its definition.

$$v(t) = \frac{\varepsilon_x(t)}{\varepsilon_y}$$

D 1

The values calculated were found to be approximately 0.45, with a significant amount of scatter in the data. The data can be seen in Figure D 3. The scatter was due to the fluctuations in temperature from the controller and the inaccuracy of DIC data at such low strains. Despite the fluctuations, the values are reasonable for the conditions and shows initial tendency towards 0.5 as the strain increases.
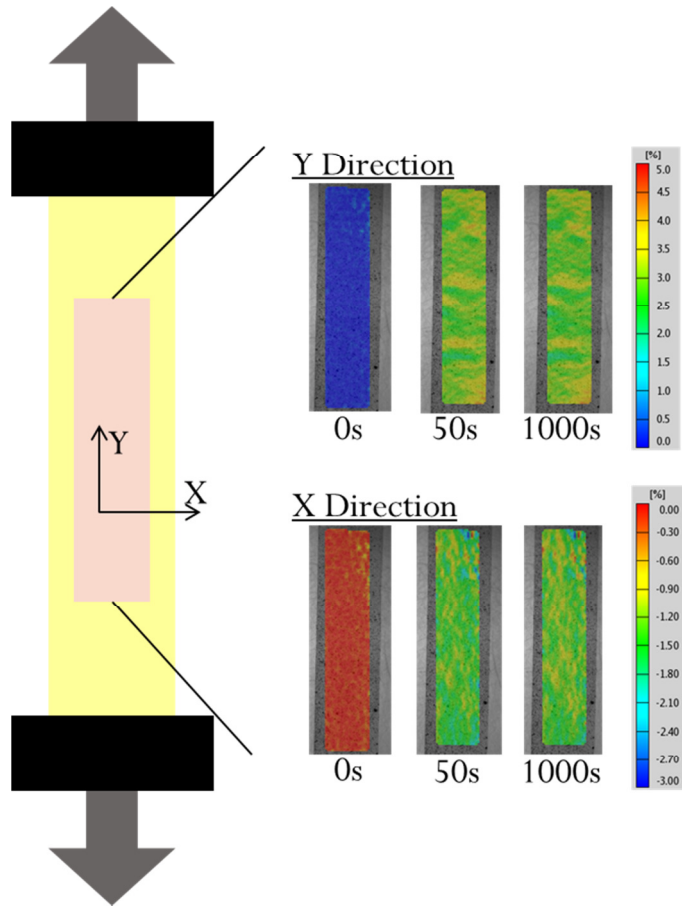
60

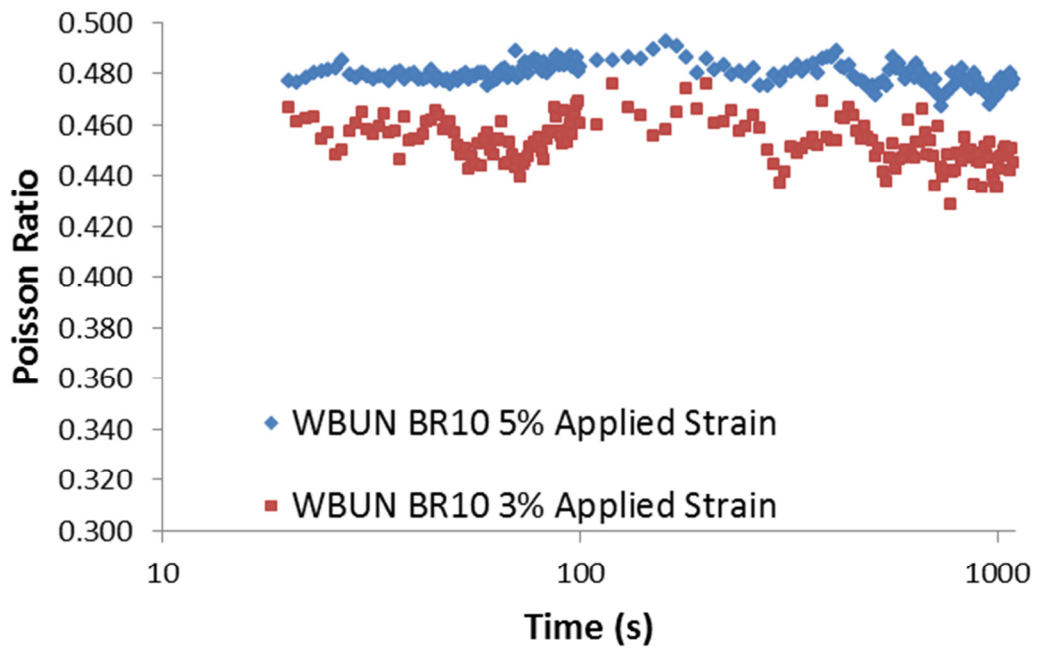**Figure D 2: DIC full field data of relaxation tests on WBUN BR10**

Figure D 3: Measured values of Poisson's ratio during relaxation testing for WBUN BR10 at 90°C and nominally dry conditions

Much of the work in stress calculation for this thesis was based on constant volume assumptions. The important question to ask is how good an approximation this is, which includes the measurement of Poisson's ratio, as well as knowing what strains the tests are occurring at. Plastic deformation is considered to be isochoric ($v \rightarrow 0.5$) and for normal materials v might drop below 0.5 if voids begin to open. For both Nafion® and TAKS115C BR10 30% Kynar Flex® the yield was found to be around 2.5% to 3% strain. Since blister strains were well above this, the isochoric approximation was considered good. As was seen in the previous figure, the Poisson's ratio was between 0.47 and 0.49 at strains of 5%.

To complete a full study, more robust measurements must be taken at lower strains, since the definition of Poisson's ratio is truly linear elastic. However, in support of this thesis, the trend towards isochoric behavior as strains increased was seen and an initial value near 0.45 was found. Both of these provide support for the constant volume approximation.

Appendix E: Apparent flow rate dependence of blister failure times

On inspection of flow right comparisons, it was found that flow rate did influence blister failure times significantly. Flow rates were controlled using needle valves attached to the blister fixture. They were not documented in terms of flow right, since that was pressure dependent, but instead by the number of turns open. 8 turns open corresponds approximately to the needle valve being set at half of max. Figure E 1 shows the comparison of blister failure times and the needle valve opening.
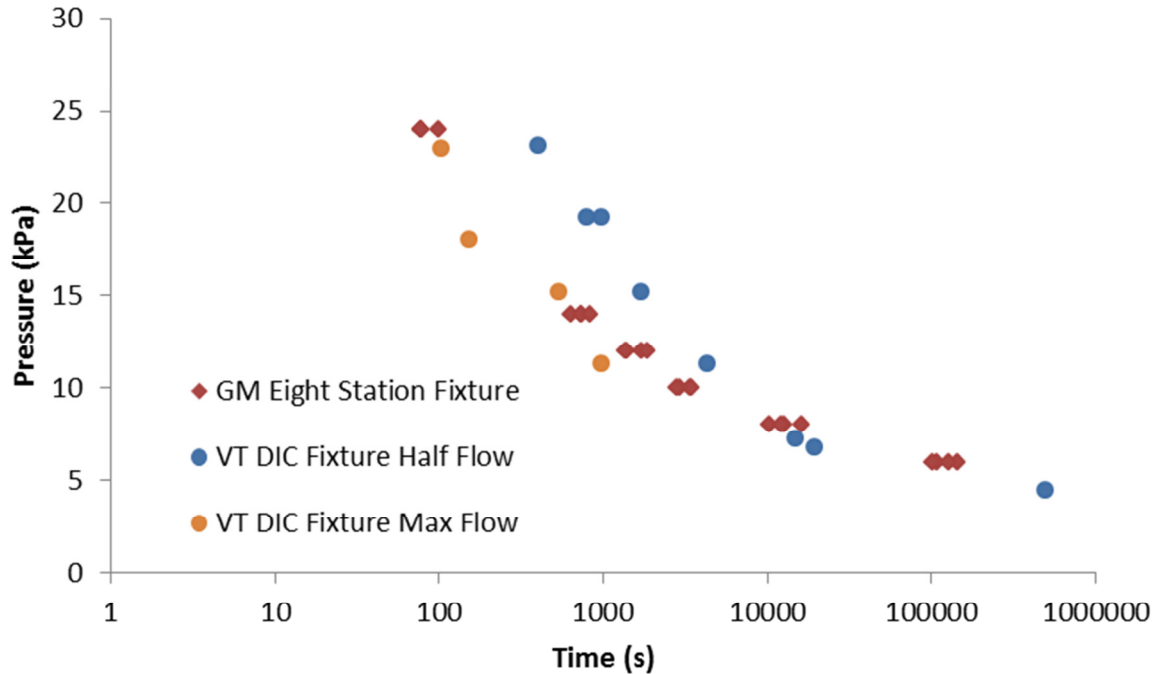

Figure E 1: Constant pressure to failure data of Gore-Select® series 57 membrane at 90°C and nominally dry conditions. This shows that the flow rate changes the failure time of the material by over half a decade at short times.

This behavior might be expected for large differences in loading times between the rates. Those differences were measured and are shown in Figure E 2 & Figure E 3. Kapton® was used at room conditions as the pressurized medium to minimize creep.
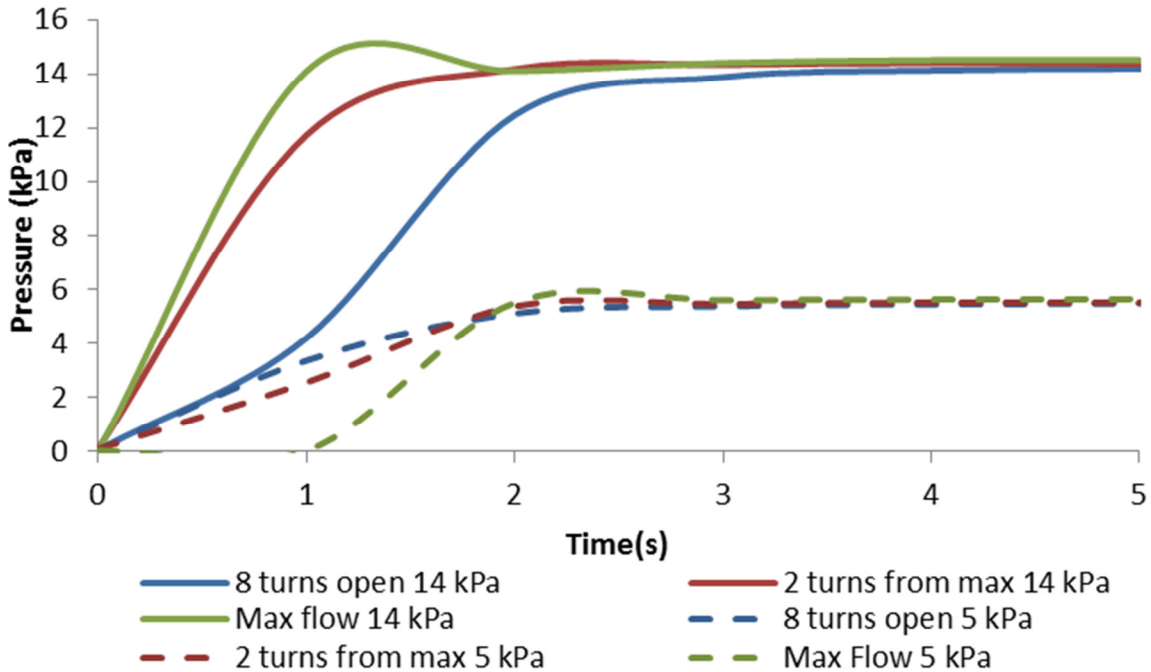
Figure E 2: Measurement of pressure data upon loading for different flow rates at a higher and lower pressure. This does not show substantial differences between the flow rates in time reaching pressure.
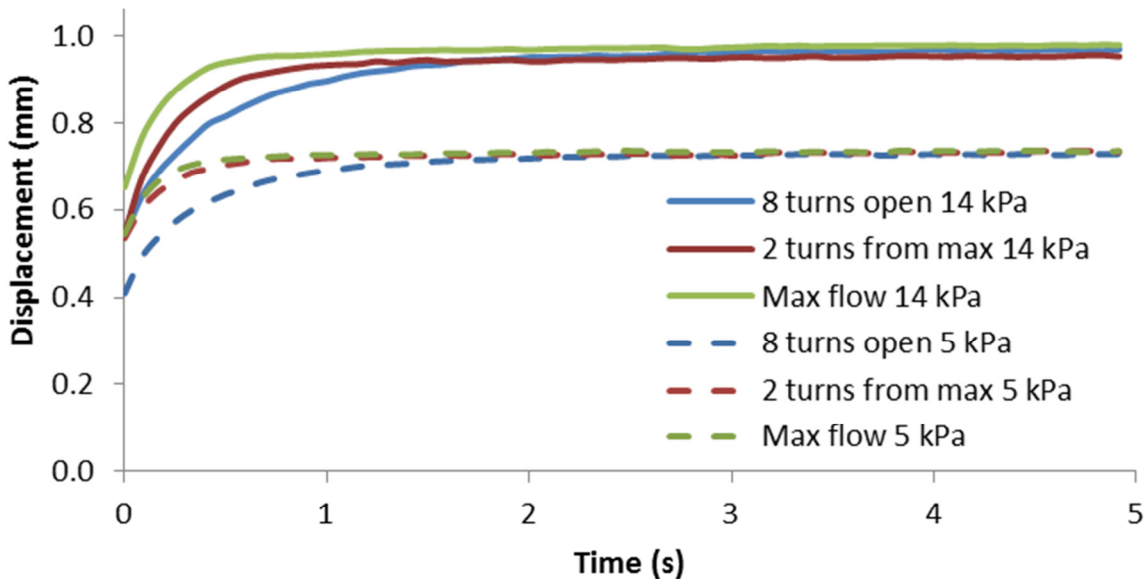

Figure E 3: Displacement versus time of Kapton® membrane showing that the max displacement and time to the max displacement is moderately dependent on flow rate, but becomes indistinguishable after 2s.

As can be seen, the pressure versus load time does not appear to show significant differences, not at least which would correspond to nearly a decade of difference in failure time. The same is shown in the displacement versus load time for the Kapton®. These results are concerning and suggest that greater effort should be put into understanding the behavior of the blister under different flow rates in the future.

Appendix F: Sensitivity of LDA predicted failure times to extrapolation technique based on Gore-Select® series 57 data

To check the sensitivity to the type of extrapolation, the A and B values used were calculated by minimizing the error with an exponential extrapolation. These A and B values were then used along with two other extrapolation functions (linear and power law extrapolations) to predict the failure of the material by numerically integrating Eqn 3.7 until the integral summed to 1. The plot below shows that the difference in predicted failure is negligible in terms of durability data. The experimental data is also plotted alongside to reference the absolute error. A and B were 4.44×10^8 and -4.85 respectively.
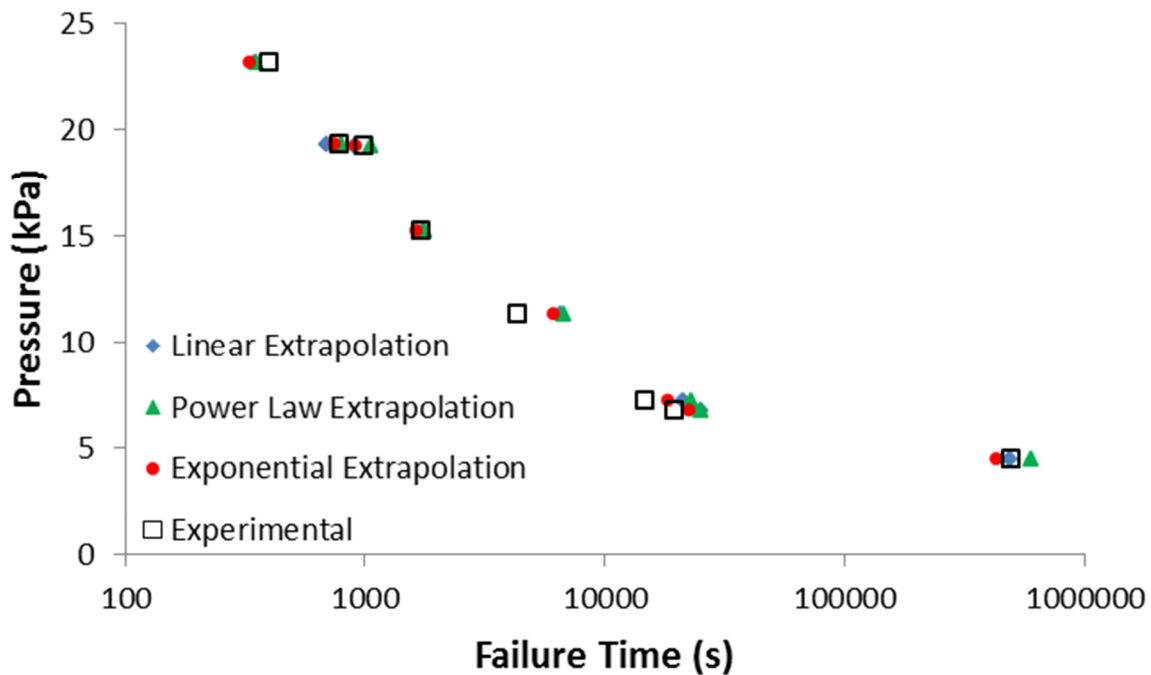

Figure F 1: Differences in predicted failure induced by the assumption of different extrapolating functions